

PALACKÝ UNIVERSITY OLOMOUC
FACULTY OF SCIENCE
JOINT LABORATORY OF OPTICS

BACHELOR THESIS

Calibration and monitoring of astroparticle
telescopes



Author: **Daniel Staník**
Study program: B0533A110007 Applied Physics
Field of study: 1702R001 Applied Physics (AFYZ)
Form of study: Full-time
Supervisor: Ing. Ladislav Chytka, Ph.D.
Deadline: April 2022

DECLARATION

I hereby declare that I elaborated this bachelor thesis independently under the supervision of Ing. Ladislav Chytka, Ph.D., using only information sources referred in the Literature chapter.

In Olomouc February 14, 2022

.....
Daniel Staník

Bibliographical identification

Autor's first name and surname	Daniel Staník
Title	Calibration and monitoring of astroparticle telescopes
Type of thesis	Bachelor
Department	Joint Laboratory of Optics
Supervisor	Ing. Ladislav Chytka, Ph.D.
The year of presentation	2022
Abstract	<p>Lorem ipsum dolor sit amet, consectetur adipiscing elit. Curabitur et lectus sit amet lectus vestibulum dignissim. Cras sit amet enim vitae mi elementum blandit eget nec tortor. Curabitur eget eros vitae arcu luctus varius commodo vel mauris. Nam elementum convallis pretium. Nunc dignissim pulvinar urna, nec blandit ante fringilla at. Ut et magna purus, vel pellentesque massa. In tortor nisi, faucibus condimentum cursus ut, sollicitudin quis leo. Ut at purus nec arcu accumsan tincidunt id id massa. Nam id vehicula mi.</p> <p>keyword 1, keyword 2, ...</p>
Keywords	
Number of pages	xx
Number of appendices	x
Language	english

Bibliografická identifikace

Jméno a příjmení autora	Daniel Staník
Název práce	Kalibrace a monitorování astročásticových teleskopů
Typ práce	Bakalářská
Pracoviště	Společná Laboratoř Optiky
Vedoucí práce	Ing. Ladislav Chytka, Ph.D.
Rok obhajoby práce	2022
Abstrakt	<p>Lorem ipsum dolor sit amet, consectetur adipisciing elit. Curabitur et lectus sit amet lectus vestibulum dignissim. Cras sit amet enim vi- tae mi elementum blandit eget nec tortor. Cur- abitur eget eros vitae arcu luctus varius com- modo vel mauris. Nam elementum convallis pretium. Nunc dignissim pulvinar urna, nec blandit ante fringilla at. Ut et magna purus, vel pellentesque massa. In tortor nisi, faucibus condimentum cursus ut, sollicitudin quis leo. Ut at purus nec arcu accumsan tincidunt id id massa. Nam id vehicula mi.</p>
Klíčová slova	klíčové slovo 1, klíčové slovo 2, ...
Počet stran	xx
Počet příloh	x
Jazyk	anglický

Contents

Introduction	7
1 Astroparticle detection	8
1.1 Cosmic rays and particles	8
1.1.1 Primary cosmic rays	8
1.1.2 Secondary cosmic rays	9
1.2 Ultra-high energy cosmic rays (UHECRs)	9
1.3 UHECRs detection techniques	10
1.3.1 Air fluorescence	11
1.3.2 Surface particle detection	11
1.3.3 Hybrid detection	12
1.4 UHECRs observatories	12
2 FAST telescope	13
2.1 FAST detection and operation scheme	14
2.2 Protection hut	15
2.3 Remote control and monitoring	15
3 Calibration of astroparticle detectors	17
3.1 Absolute calibration	17
3.2 Relative calibration	17
3.3 FAST calibration	18
3.3.1 Flasher	18
3.3.2 YAP pulser	18
3.3.3 Homogeneous light source	18
3.3.4 Drone with light source	18
4 Instrumentation and measurement methodology	19
4.1 Integration sphere	19
4.2 Photomultiplier tube	20
4.2.1 Operating principle	20
4.2.2 Dark current	23
4.2.3 Timing and response	24
4.2.4 Operating life and degradation	24
4.3 Hardware for experiment control	24
4.3.1 Raspberry Pi	24
4.3.2 STM32 based microcontrollers	24

5 Calibration UV optical source	25
5.1 UV source	25
5.2 Testing and measurement of UV source	27
5.2.1 Measuring apparatus	27
5.2.2 Data acquisition and analysis	29
5.2.3 Results	31
5.3 UV LED diode ageing	35
5.4 Optical feedback - potential fix	36
5.4.1 Detection photodiode	36
5.5 Modified UV source for drone mounting	42
6 Monitoring system	43
6.1 Monitoring of multiple FAST telescopes	43
6.2 Control units and sensors	43
6.3 Software system	45
7 Calibration data analysis	47
7.1 Calibration process	48
7.2 Analysis and results	49
7.3 Simulation compartment and discussion	52
Conclusion	53

Introduction

Lorem ipsum dolor sit amet, consectetur adipiscing elit. Curabitur et lectus sit amet lectus vestibulum dignissim. Cras sit amet enim vitae mi elementum blandit eget nec tortor. Curabitur eget eros vitae arcu luctus varius commodo vel mauris. Nam elementum convallis pretium. Nunc dignissim pulvinar urna, nec blandit ante fringilla at. Ut et magna purus, vel pellentesque massa. In tortor nisi, faucibus condimentum cursus ut, sollicitudin quis leo. Ut at purus nec arcu accumsan tincidunt id id massa. Nam id vehicula mi.

<http://exfyz.upol.cz/didaktika/>

Chapter 1

Astroparticle detection

More than 100 years have passed since Victor Franz Hess first encountered cosmic radiation. Since those times the techniques and methods of detection have been strongly improved. We have moved up from elevating electroscopes by balloons to observe growing electric charge to specialized techniques, which allows us to measure particles' energies, trajectories, etc.

1.1 Cosmic rays and particles

Cosmic rays is a term for radiation and energetic particles striking earth atmosphere with an origin in a outer space sources (neutron stars, supernovas, black holes, etc). There are two types of cosmic rays - primary and secondary. Primary cosmic rays are the original cosmic particles, which strike the Earth's atmosphere. Secondary cosmic rays (also referred as showers) are particles, which have origin in particle interaction between primary cosmic rays and the atmosphere.



Figure 1.1: Illustration of cosmic rays striking Earth's atmosphere (credit: A. Chantelauze, S. Staffi, L. Bret) [12].

1.1.1 Primary cosmic rays

Primary cosmic rays consist of protons (95%), helium nuclei (4%), electrons and other heavy nuclei (up to iron). However, only the highly energetic rays make their way to the atmosphere. The Earth's magnetic field affects their trajectories and prevents the low-energetic (less than 100 MeV) particles from arriving to the atmosphere [9].

Part of primary cosmic rays are also Ultra-high energy cosmic rays (UHECRs), which we refer to in the next chapter.

Neutrinos are also a part of cosmic radiation, but their interaction with matter is very rare, so they are very hard to detect. The special underwater detectors are developed to detect some of them.

1.1.2 Secondary cosmic rays

Secondary cosmic rays are created by interaction of high-energy particles of primary component with air nuclei, such as nitrogen. They consist of low-energetic and high-energetic muons, gamma photons, electrons and positrons. Most of muons travel up to the earth's surface although their half-life is only about 2.2 microseconds before they decay into electrons and neutrinos. Due to their high relativistic speeds, their half-life is increased for external observers.

1.2 Ultra-high energy cosmic rays (UHECRs)

UHECRs are particles with energies from 10^{18} to 10^{20} eV, which is much more than particles created on CERN's Large hadron colider (LHC) with energies about 10^{13} eV. Due to their high energies, the trajectory remains nearly unchanged by space magnetic fields [14].

UHECRs' origin is yet unknown, but it is supposed and experimentally proven that they come from outside of the Milky Way. Some theoretical physicists expect, that the one possible source of UHECRs acceleration are the starburst galaxies. One of UHECR possible particle is proton.

In many particle physics experiments, some form of calorimeter is used to determine the particles' energy and direction. In case of UHECRs, the air molecules of atmosphere have the function of calorimeter. When UHECR interacts with atmospheric nuclei, the cascade of particles is induced. This cascade consists of three main components: electromagnetic, hadronic and muonic. It is also referred to as extensive air shower (EAS).

In case of ultra-high energy proton striking an air molecule, kaons, baryons, nuclear fragments and mostly pions are created. Together, they are referred to as hadronic component. The pions with short lifetime decay into electromagnetic sub-shower. The behaviour of pions with longer lifetime is energy-dependent. At higher energies they reinteract with atmospheric nuclei and feed hadronic and electromagnetic component. At lower energies they decay into muonic component with muonic neutrinos. The muons with short lifetime decay into electrons and positrons with neutrinos, which join the electromagnetic cascade, while the others reach the Earth's surface carrying the energy, which we are unable to detect (invisible energy). The UHECR's cascade scheme is shown in Fig. 1.2.

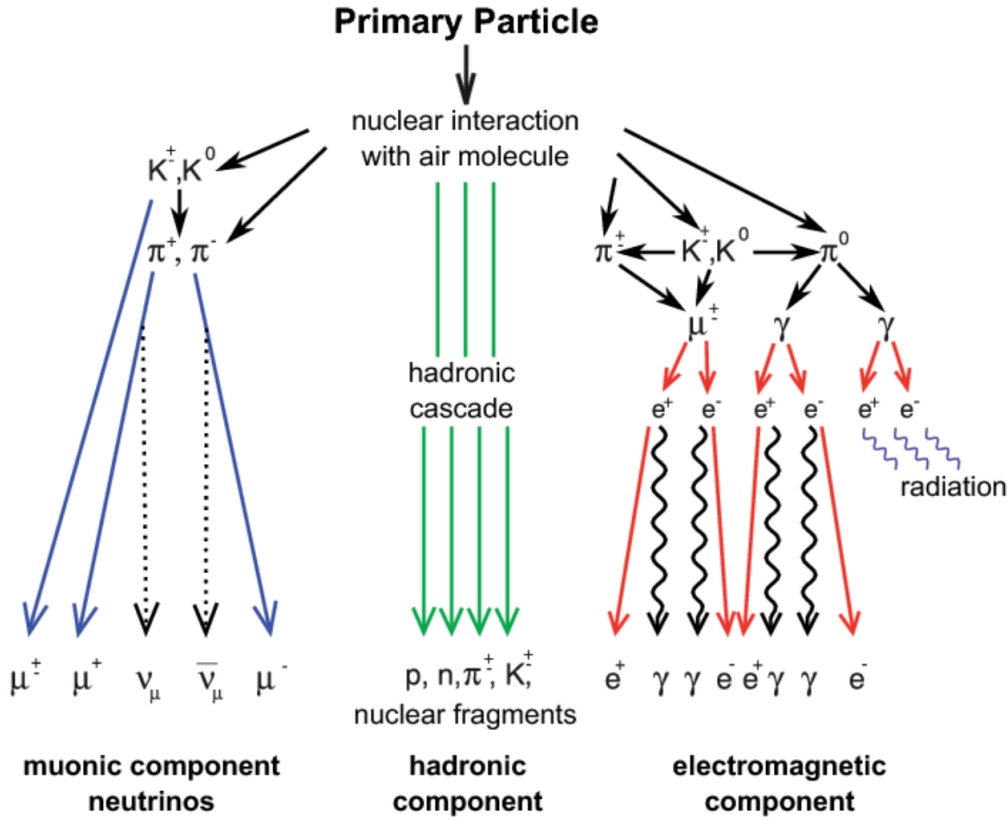


Figure 1.2: UHECR's cascade, taken from [3].

The electromagnetic cascade consisting of electron, positrons, gama photons carries the most of UHECR's energy. With increasing depth, the cascade develops by decaying the photons into electron and positron pairs, which again emit photons and this process repeats. The cascade develops until the the energy treshold is reached, where the ionization is higher than the radiation losses. [1].

Every UHECR shower has its own longitudinal profile. One of the main parameters of this profile is X_{max} - the point along the shower axis, where the maximum of deposited energy is. Other property which we are able to capture is the lateral distribution of particles, which has a decreasing trend with the increasing distance from the shower core. By analysing the signal waveforms from our detectors we are also able to determine the time structure of the event.

1.3 UHECRs detection techniques

Nowadays there are three main proven techniques to detect UHERCs - air fluorescence, surface particle detection and Cherenkov light detection. Typical detectors consist of the optical part (mirrors, reflectors, optical filters and water/scintillator), the detection part (PMTs and PMT based cameras) and the electronic part. The electronic part mainly consists of special triggering and sampling systems and a data acquisition system (DAQ) capable of storing huge amounts of complex data (full signal waveforms etc.).

1.3.1 Air fluorescence

The electrons and positrons from electromagnetic cascade excite nitrogen molecules, which then deexcite and emit fluorescence UV light in with two main wavelengths 337 and 357 nm. The intensity of this light is directly proportional to the calorimetric energy of the shower.

However, the intensity of this light is very low, and thus the measurements must be done in dark nights with no light smog. Even a low intensity of external sources can lead to detection of false events or worse - the unwanted light may damage the very sensitive equipment.

The detection equipment consists mostly the superreflective UV mirrors which focus part of the UV shower into the PMT or into the camera based on PMTs. It is necessary to have atmospheric monitoring system (temperature, humidity, pressure etc.) along with the detection part, because the fluorescence is highly dependent on these conditions.

The main advantage of fluorescence detection is the fact, that by measuring and integrating the light profile we are able to calculate the total calorimetric energy. However, corrections must be made due to the invisible energy.

The FAST telescope, on which we focus in this thesis, is a fluorescence telescope.

1.3.2 Surface particle detection

Surface particle detection is a method, which is based on detecting individual particles from EAS. There are two proven surface techniques to detect EAS - by scintillators or water Cherenkov detectors. To detect the EAS full geometric distribution, huge surface needs to be covered by surface detectors. By combining the information from the multiple surface detectors we are able to obtain the footprint, direction and the total energy of the air shower.

In case of Cherenkov surface detectors, the special plastic tanks filled with purified water are used. The water is used as a Cherenkov radiator, which emits the Cherenkov photons whenever the relativistic charged particle strikes the detector. This light is sampled by PMTs overseeing the water. To increase the collection efficiency, the tank's inner surface is covered by reflective material. The detector is also sensitive to the non-Cherenkov high energetic photons, which has the origin in the electron and positron annihilation in the UHECR's cascade.

The second possibility is to use the detectors equipped with scintillators. Scintillator detectors are flat devices with a scintillator array in a metal clad. The scintillator consists of special molecules which are sensitive to charged particles, which are excited when struck by a charged particle. Upon deexcitation they emit UV light which is transferred to PMTs by optical fibers.

Compared to fluorescence detection method, the surface detectors don't require the dark night and any light exposure is not a threat for them. Thus they are capable of operating during the entire day.

The main disadvantage of surface detection is the calibration. For solo surface detector, there is only one possibility - by using simulation models, which are mostly corrupted by many uncertainties. Better approach to solve this problem is to use the hybrid detection technique.

1.3.3 Hybrid detection

Nowadays the hybrid detection seems to be the most proven way to detect UHECRs. Both of the main UHECRs observatories - the Pierre Auger observatory and the Telescope array project both are based on the hybrid detection.

The hybrid detection allows the observatory to operate 100 % of the daytime and mainly solves the surface detector calibration problems. By comparing the event captured by both fluorescence and surface detectors we are able to transfer the energy scale from the fluorescence detectors to the surface detectors and thus calibrate the surface detectors.

1.4 UHECRs observatories

The Pierre Auger observatory is the observatory located on the southern hemisphere. It uses over 1660 Cherenkov tanks as surface detectors covering more than 3000 km^2 of the Pampa Amarilla. 27 telescopes situated on the boards of the observatory are used as fluorescence detectors [1].

The Telescope array project is located on the northern hemisphere in Millard County, Utah. It consists of more than 500 scintillator detectors and three fluorescence telescope stations [11].

Chapter 2

FAST telescope

The Fluorescence detector Array of Single-pixel Telescopes (FAST) is an international project of fluorescence telescope sensitive to UHECRs.

Until today there are four prototypes in active service. Three of them are situated in Black Rock Mesa site of the Telescope Array experiment in central Utah and one in Argentina near Pierre Auger Observatory.

The main goal of FAST project is to develop a cheap fluorescence telescope, which could be used in future to cover a wide surface area. This new oncoming fluorescence telescope array should be able to fully reconstruct the geometry of UHECRs induced UV shower by combining the information from the multiple telescopes.

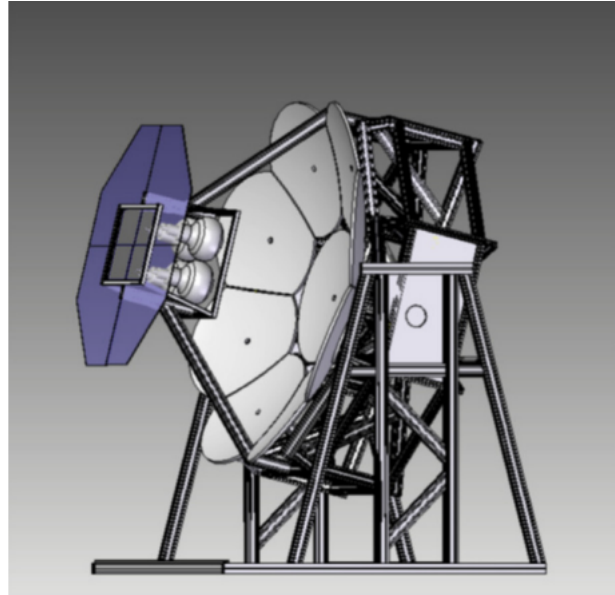


Figure 2.1: FAST telescope's design [4].



Figure 2.2: FAST telescope [7].

2.1 FAST detection and operation scheme

Main detection part of telescope consists of system of superreflective UV mirrors and 2x2 20cm PMT matrix (detection camera). The full specification of FAST optical concept could be found in [2] and [4].

The mirror system consists of primary circular mirror and 8 smaller side mirrors (called petals), which focus the rays into detection camera. The camera is located 25 mm away from the focal plane further from the mirror to prevent the on-axis rays to focus in the dead space between PMTs. This concept gives FAST collecting area of 1 m^2 and a FoV (field-of-view) of $30^\circ \times 30^\circ$. On the fig. 2.3 could be seen the simulation of the optical concept.

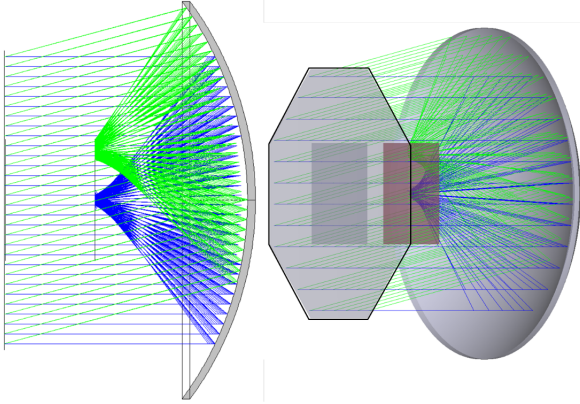


Figure 2.3: Simulation of the FAST optical concept [2].

The aperture is covered by UV filter, which blocks the night-sky background photons ($\lambda > 400$ nm) and protects the mirrors.

The NIM module provides a stable, low noise high voltage (900 - 1000 V) for all 4 PMTs, adjusting their gain around 10^5 . To establish same signal responsivity the different voltage can be adjusted to every single PMT.

The data acquisition is handled by single-board PC, which runs the data acquisition software (DAQ). The DAQ controls the 14-bit FADC, which samples the pulses at rate 50 MSamples/s. The sampling can be triggered by internal high-threshold trigger or by external signal. Time stamps are provided by GPS module. The raw data are stored in format containing signal waveforms, which can be later converted into the ROOT format, which we use in analysis.

2.2 Protection hut

The entire telescope along with monitoring systems and other instruments is situated in a hut with remote shutter, where it is protected from adverse phenomena, such as rain or fast wind, but also from dust and aerosols. Exposure of mirrors to any of this phenomena could lead to reduction of theirs reflectivity. It is also necessary to monitor and protect PMTs from unwanted light sources. Even a low-intensity sources could decrease PMT's service life.

2.3 Remote control and monitoring

In case of Argentina prototype, the telescope's systems are connected to Pierre Auger network and through it, the telescope can be fully remote controlled and monitored over the internet.

Testing measurements, usually referred to as shifts, are performed in the night. Their main purpose is to acquire data, which can be later analysed and compared with data from Los Leones part of Pierre Auger, which has the similar FoV as Argentine FAST. The testing measurements require an operator to look after the telescope systems. An operator's duty is to power on and off the DAQ, PMTs' voltage sources, perform calibration, open and close the shutter and mainly check for failures and negative phenomena. To do that, operator can access webcam (2.4), meteostation with thermometers, humidity, wind and light sensors and the Allsky camera.



Figure 2.4: FAST telescope with the opened shutter from the webcam.

Chapter 3

Calibration of astroparticle detectors

Calibration is a process, which we perform to obtain relationships between measured values by tested device and values given by ethalon. These relationships may be specified by calibration constants, functions or by other mathematical relations. The tested devices can be also calibrated relatively to each other.

3.1 Absolute calibration

The term absolute calibration can be specified as a measurement process, which results in obtaining reference between the detector's responsivity and the defined value of some physical quantity induced by an external source. In case of detectors consisting of PMTs or PMT based cameras it is reference between optical power seen by detector and its output photocurrent. Due to the PMT's linearity principle we can define this reference by one constant for every PMT or pixel. However, in real applications, other corrections must be made.

Good example of absolute calibration are large-aperture light drums, which are used at Pierre Auger for fluorescence telescopes calibration. The drum's inner surface is coated with a diffuser and an UV LED is used as a light source with defined power. This concept provides a homogeneous intensity for absolute calibration of large mirrors along with the PMT camera.

In many cases the absolute calibration is a complicated process, and thus it is done less frequently than the relative calibration.

3.2 Relative calibration

The term relative calibration refers to comparing the response on the same signal between two detectors or to propagating the constants from absolute calibration over time. In this thesis we mainly use this term to describe the comparing the signal response between PMTs, which belong to the same FAST telescope.

The relative calibration has a lesser requirement on instruments and methods than the absolute calibration. For example we don't have to illuminate the PMTs with well defined intensity, the only requirement is to illuminate each of them with the same amount.

3.3 FAST calibration

FAST telescope calibration techniques are yet under development. It is necessary to calibrate PMTs both in absolute and relative way, but also the entire telescope as optoelectronic system with mirrors and PMTs. However, the mirrors also suffer from various effects, and thus their reflectance needs to be tested sometimes.

3.3.1 Flasher

As was mentioned before, the FAST telescope is equipped with UV LED flasher, which is used to generate light pulses. Relative calibration of PMTs by flasher is performed during every shift.

3.3.2 YAP pulser

YAP pulser consists of radioactive isotope of Am-241 and YAP scintillator crystal. Due to the long half life of Am₂₄₁, the YAP pulser could be used as stable low-intensity UV source. It is mainly used for absolute calibration of PMTs. During the calibration the YAP pulser is mounted directly on the window of the PMT.

3.3.3 Homogeneous light source

Another way of calibration is to use a stable light source mounted into the IS. However, this homogeneous light source is not able to produce homogeneous illumination for the entire FAST's aperture.

To perform a relative calibration with the mirrors and the entire optical system included, it would be necessary to XY scan the aperture with the homogeneous light source, but this would be very difficult to implement.

The other and more practical way is to illuminate the telescope's aperture from few different positions and obtain relative responsivity ration constants for every PMT (not final calibration constants). By comparing these measured responsivity ration constants with its theoretical counterparts produced by simulations of illuminating the FAST's optical system, we are able to calculate the relative calibration constants for every PMT.

The analysis of calibration data acquired by this method are presented in chapter Calibration data analysis.

As a light source for this application is used thermal stabilized UV LED source. The functionality and testing of this source is more discussed in chapter 5.

3.3.4 Drone with light source

There is a possibility to use a drone to carry the calibration light source. Performing this type of calibration will allow us to scan the FAST's FoV homogeneity from the air. However, this type of calibration is yet under fresh development and has never been performed on the FAST yet. In this thesis at the end of chapter 5 we focus on the development of some prototype parts for drone.

Chapter 4

Instrumentation and measurement methodology

To perform all of necessary measurements we need to use various types of optical and electronic equipment.

4.1 Integration sphere

The Integration sphere (IS) is a special optical equipment, which can be used either as extended uniform light source (EULS) e.g. with spectrometer in determining the material reflectance. In our experiments we use general purpose Labsphere (Fig. 4.1).



Figure 4.1: General purpose Labsphere.

The IS inner surface consist of white optical diffusive material (BaSO_4 and Poly-tetrafluoroethylene). The IS also contains several circular apertures, which are called

input/output ports. These can be used to mount detectors or optical sources or left free to let light flux enter or exit IS.

The inner surface is part where light integration happens. The effect which takes place here is known as Lambertian scattering. After one spot of inner surface is hit by a ray, the energy should be uniformly radially distributed. In output port this produces a homogeneous light source. The homogeneity decreases with increasing number and sizes of input/output ports.

Using optical source with IS requires baffle to prevent source's light flux or its part to exit IS without integration.

More deeper explanation of IS working principles and characterization of optical properties of the identical IS, which we use, can be found in [5].

For our purposes, in case of FAST calibration, we use IS as an UV EULS. In case of testing optical UV calibration source, we use IS mainly to block the possible incoming external light and to distribute the optical power of the UV source between mounted detectors.

4.2 Photomultiplier tube

Photomultiplier tube (PMT) is considered to be a high voltage optoelectronical part. It allows us to measure very low intensity optical signals. PMT is also characterized by high amplification, low noise and stability. It has many variants of usage. It can be used either as detector of optical signal (pulse or continual) for chosen wavelength or as a radiation detector. We can construct a counter or a multichannel analyzer by mounting an appropriate scintillator on the window of the PMT. The general theory of PMTs is described in more detail in [8, 10].

4.2.1 Operating principle

PMT consists of 6 main elements, which can be seen on scheme 4.2.

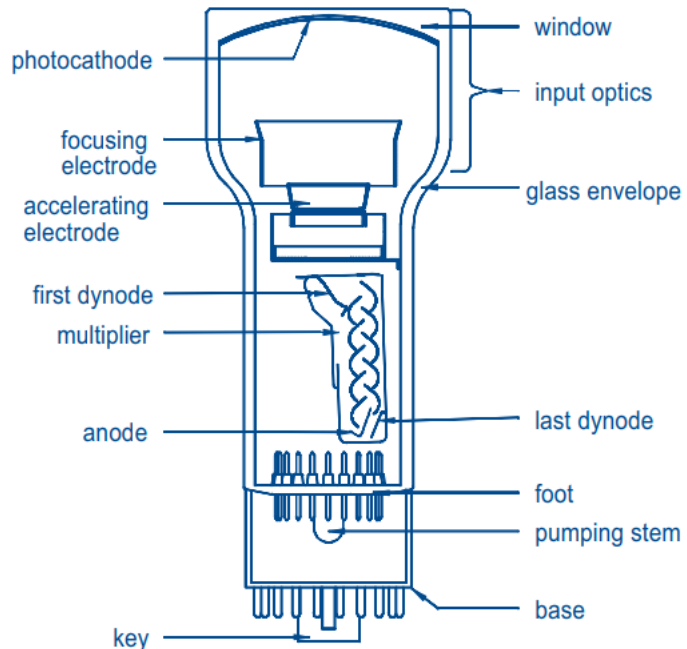


Figure 4.2: Photomultiplier tube scheme [10].



Figure 4.3: XP2262 PMT used for our measurements.

The input photon with sufficient energy, which strikes the PMT's photocathode, excites photocathode's electron. This electron then follows electrostatic field to the first dynode of the electron multiplier, where it induces secondary emission of more

electrons. These electrons are then attracted by the next dynode, where the emission process repeats. After few times of multiplying electron number over dynodes, the electrons are then collected by the anode, which is situated on the end of the electron multiplier. The anode output current is then converted to voltage signal by appropriate load resistor or by operational amplifier current-to-voltage circuit.

As all other laboratory instruments, which are based on accelerating electrons, such as electron microscopes, the photomultiplier's main parts must be kept in vacuum. To maintain vacuum, the photomultiplier is surrounded by special glass envelope. To avoid mechanical damage of the glass envelope, the entire photomultiplier is situated in a plastic tube.

One of the basic adjustable characteristic of PMT is its gain. The gain is defined as:

$$G = \frac{I_a}{I_p}, \quad (4.1)$$

where I_a is the anode current and I_p is the input photocurrent from the photocathode.

In case of ideal, noiseless PMT, we can adjust gain by varying the supply voltage. By varying supply voltage we can adjust gain according to an equation:

$$\frac{G_2}{G_1} = \left(\frac{V_2}{V_1}\right)^{\alpha N}, \quad (4.2)$$

where G_2 and G_1 are gains at supply voltages V_2 and V_1 . α is coefficient given by dynode material and N is the number of dynodes.

Other effects, such as temperature, may also vary PMT's gain, and it is necessary to keep them on constant value or measure them and involve them in the final evaluation of data.

For proper functionality of the PMT, the charge and current linearity should be considered. Charge linearity is the ratio of the number of incident photons to the number of electrons collected at the anode. Current linearity express the proportionality between incident light flux and anode current. Ideal PMT is always linear, but the real PMT may vary from linearity due to drifts, space charges, instability of voltage divider etc. These effect can lead up to saturation of the PMT. In saturation, increasing the input light flux leaves the anode current mostly unchanged.

Window

The photocathode is coated on glass window, whose main purpose is to admit light of certain wavelengths. Glass materials are characterized by the spectral sensitivity to wavelengths. For transparency in UV spectre, it is advised to use borosilicate or fused silica glasses.

Photocathode

The photocathode is the only light-sensitive part of PMT. It transfers the light flux into the electric current.

One of its main parameters is quantum efficiency. It is referred to as ratio of emitted photoelectrons to the number of incident photons expressed as a percentage. It is generally less than 35 %. For measurement, the more practical parameter is cathode radiant sensitivity. It is the ratio of photocathode current to an incident light power, which is expressed in mA/W.

Photocathode material must be sensitive to certain wavelengths, which we want to detect with the PMT, and must have sufficient quantum efficiency. Preferred materials are usually alkali antimodes.

Electron multiplier

The electron multiplier consists of dynodes and one anode. Dynodes are electrodes, which produce more electrons through secondary emission. To maintain electrostatic field between dynodes, each of dynodes is held on different potential. This is achieved by using the voltage divider. Every resistor in the divider sets the potential of one diode according to its resistivity.

All of the photoelectrons emitted by photocathode should be ideally collected by the first dynode. However, many of them could be diverted from their path to dynode due to various effects. The parameter, which characterizes this, is the collection efficiency. The Collection efficiency is a probability that photoelectron will strike area of the first dynode.

There are few types of dynodes arrangements. On the fig. 4.2 is the classic linear-focusing multiplier.

Voltage divider and voltage adjustment

Voltage divider could be a simple resistor serial network, which divide high input voltage between the dynodes.

It is necessary to consider, that the multiplier current density increases in direction to the anode, so it tends to lessen the voltage between last dynode and anode. This phenomena can shake the potential levels across the entire multiplier. One way to reduce the impact on PMT's behaviour is to choose the proper resistor values of the divider.

The resistor values could same for all the dynodes, but for some applications it is better to have progressive voltage distribution, which increases from cathode to anode, or intermediate distribution with highest values on the beginning of the multiplier.

In some applications, where high anode current peaks are expected, the divider can be filled with reservoir capacitors, which prevent the temporally charge exhaustion of the dynodes. In pulse mode, the unwanted oscillations on dynodes may occur, in that case, it is desirable to connect additional damping resistor to the divider.

Voltage supply should be stable during the PMT's operation. As was mention before, the PMT's gain is voltage dependent. To adjust sufficient gain, high voltage (thousands of volts) needs to be applied between photocathode and anode. The high voltage needs to be ramped on required level gradually to avoid negative consequences of transition and dark current effects, which can decrease the operating life of PMT. The same truth is for shutting down the PMT.

The high voltage could be applied to the PMT in negative or positive polarity. In case of positive polarity, the cathode is held at ground and anode on +HV. In case of negative polarity, the cathode is held at -HV and anode at ground.

4.2.2 Dark current

Dark current is anode current produced by photomultiplier in total darkness. It is considered to be a part of unwanted noise, causes errors in measurements and limits the detectivity of PMT. Dark current has origin in ohmical leakage, thermionic and

field emission or in radioactivity. Ohmical leakage is major part of dark current at low gain. With the increasing gain the thermionic emission prevails. At high gains the field emission becomes the major part.

4.2.3 Timing and response

Differences of photoelectrons' trajectories from the cathode to the first dynode lead into time distortion of signal. For example if we were able to produce delta-function pulse, the PMT would detect pulse with some response width time t_w . With respect to differences in electron trajectories and arrival times, the PMTs are divided into 3 types:

1. **Very-fast tubes** - photoelectrons arrive simultaneously, low collection efficiency.
2. **Fast tubes** - compromise between timing performance and collection efficiency
3. **General-purpose tubes** - simple optoelectronics, good collection efficiency, low timing performance

4.2.4 Operating life and degradation

The operating life of PMT is defined as the time required for anode sensitivity to be halved. If we neglect the outside effects, the operating life mainly depends on anode current. Degradation processes start to show themselves at currents higher than $10 \mu\text{A}$. Ageing is accompanied by increasing or decreasing gain at stable voltage. Operating life of PMT is measured in thousands of operating hours.

By exposing PMT to bad conditions, such as humidity, mechanical stress, high temperatures or the high-intensity light, the PMT's operating life could be shorten much faster.

4.3 Hardware for experiment control

4.3.1 Raspberry Pi

Raspberry Pi (RPi) is a single board computer which we use mainly for the experiment control. The linux-based Raspbian or DietPi operating system allows us to easily run various scripts and programs written in multiple languages. By having wifi and an ethernet port, the RPi can be easily accessed over internet. It can be used to control instruments and data acquisition over its USBs, 1-Wire and I2C etc. However, it doesn't have any analog inputs/outputs such as ADCs and DACs.

4.3.2 STM32 based microcontrollers

For other types of tasks, which do not require data storage and remote control, but require for example an analog sampling, setting up the voltage levels or generating well defined PWM pulses, we use STM32 based microcontrollers.

For this thesis purposes we use the STM32 nucleo F411RE and the STM32 nucleo F446RE with better analog inputs/outputs.

Chapter 5

Calibration UV optical source

As was mentioned before, the calibration UV optical source is an essential instrument to perform calibrations. Its main purpose is to deliver stable intensity which does not vary over time or due to the changes in outer conditions.

In case of FAST the process of calibration requires low-intensity UV light to be delivered in microsecond square pulses. This is because FAST is a low-intensity detector and its PMTs may be easily saturated.

5.1 UV source

For the calibration purposes was developed a prototype of pulse UV source based on the current-driven LEDs inspired by the Karlsruhe Institute of Technology (KIT) concept. The active parts - LED drive circuit and 3 LEDs are situated in temperature stabilized head.

The source is driven by STM32 board, which allows us to set parameters - LED current, PWM duty and frequency.

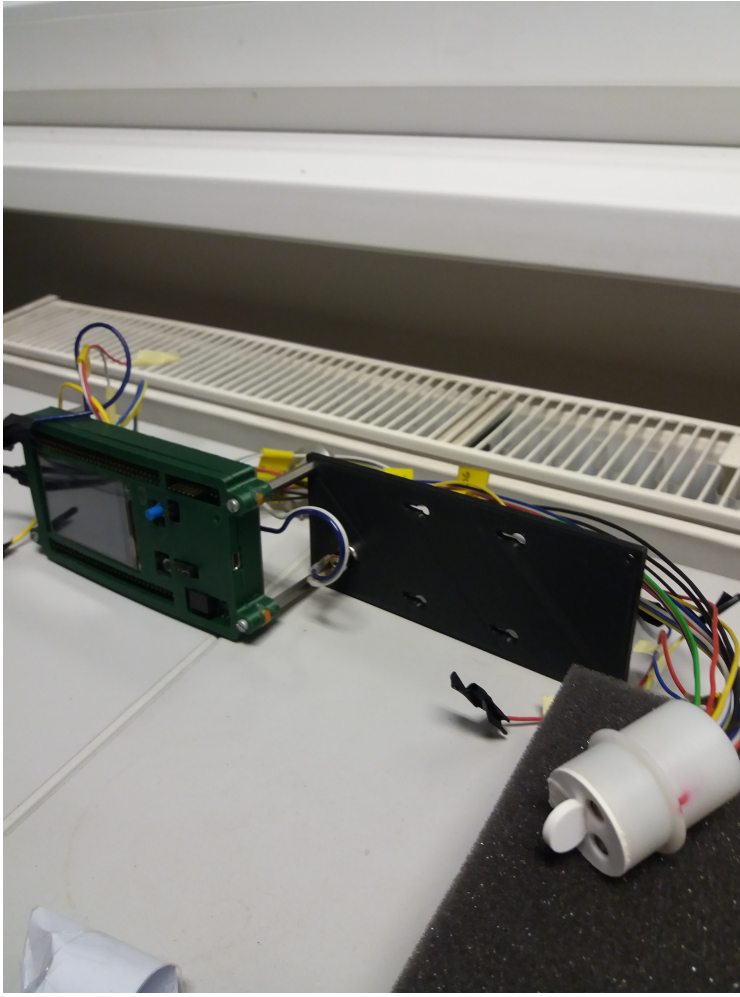


Figure 5.1: UV source constructed by Vladimír Urbášek from SLO.

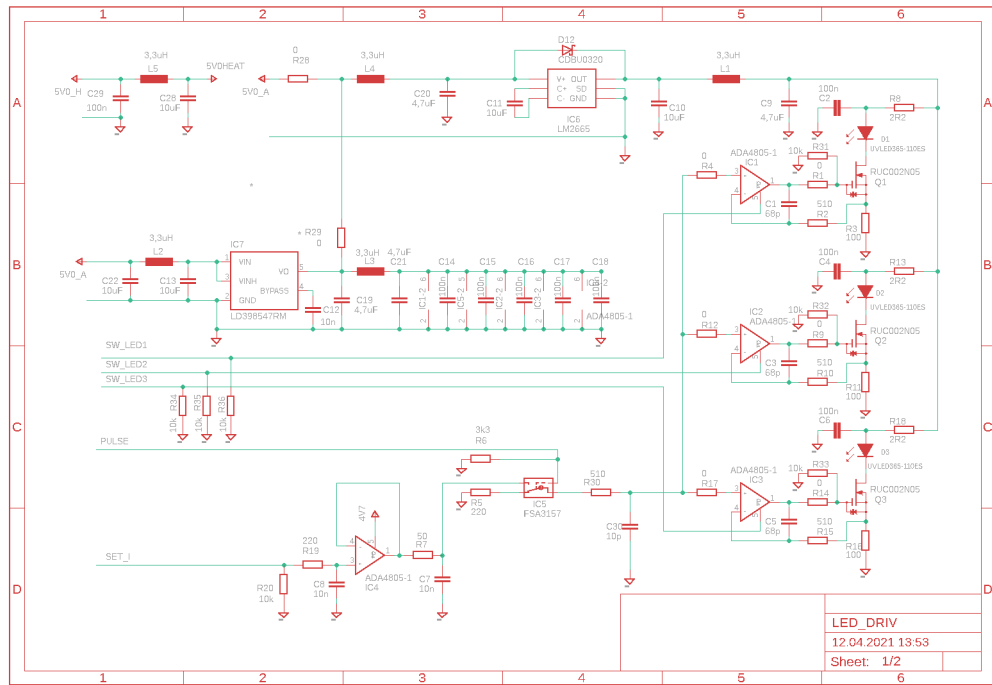


Figure 5.2: UV source schematic. On the right side we can see the pulse current drivers for three LEDs with the feedback Op amps as the main component.

Our main task was to test this UV source's long-time stability and develop possible fixes and upgrades.

5.2 Testing and measurement of UV source

For calibration UV source, the long-time stability of optical power and pulse geometry is very important. Because there was no specialized apparatus for this measurement, we had to make our own. For these measurements, we use UV source with LED current $I_d = 2.5$ mA, 50% duty cycle and frequency $f = 50$ kHz.

5.2.1 Measuring apparatus

For measuring the optical power we use PM16 power meter (PM) and for determining the pulse geometry we use XP2262 PMT with signal output connected to 2-channel PicoScope 2205A MSO usb oscilloscope. XP2262 PMT is held on $U \approx -680$ V by HV voltage source. The PMT's gain may drift over time, but we use PMT mainly for geometry analysis and measurement of absolute optical power is left to PM16.

We also use DS18B20 thermometer for PMT temperature monitoring and keysight 34461a multimeter for readout voltages.

The PMT, power meter and the optical head of UV source are mounted in the IS's ports. The IS stops the unwanted external light and distributes the optical power to PMT and power meter.

The entire apparatus is driven by Raspberry Pi (RPi). The RPi takes care of data acquisition and can be used to set the parameters of the UV source. It can be easily accessed over internet for data download or for user to control the experiment.

Oscilloscope's readout was programmed in C language according to its programmer's manual [15]. It is capable of 2ns sampling which is enough to capture rising edges of the pulses. The RPi sets basic parameters (DC coupling, range etc.) and then activates oscilloscope's trigger (rising edge). After sampling, RPi receives all samples from oscilloscope's memory.

The multimeter is controlled by VISA commands using python USBTMC library. For thermometer we use RPi's 1-Wire.

Main component (IS,PW, PMT with HV source, UV source) are situated in protection box to prevent unwanted manipulations and touching the HV parts. The apparatus can be seen on fig. 5.3 and 5.4.

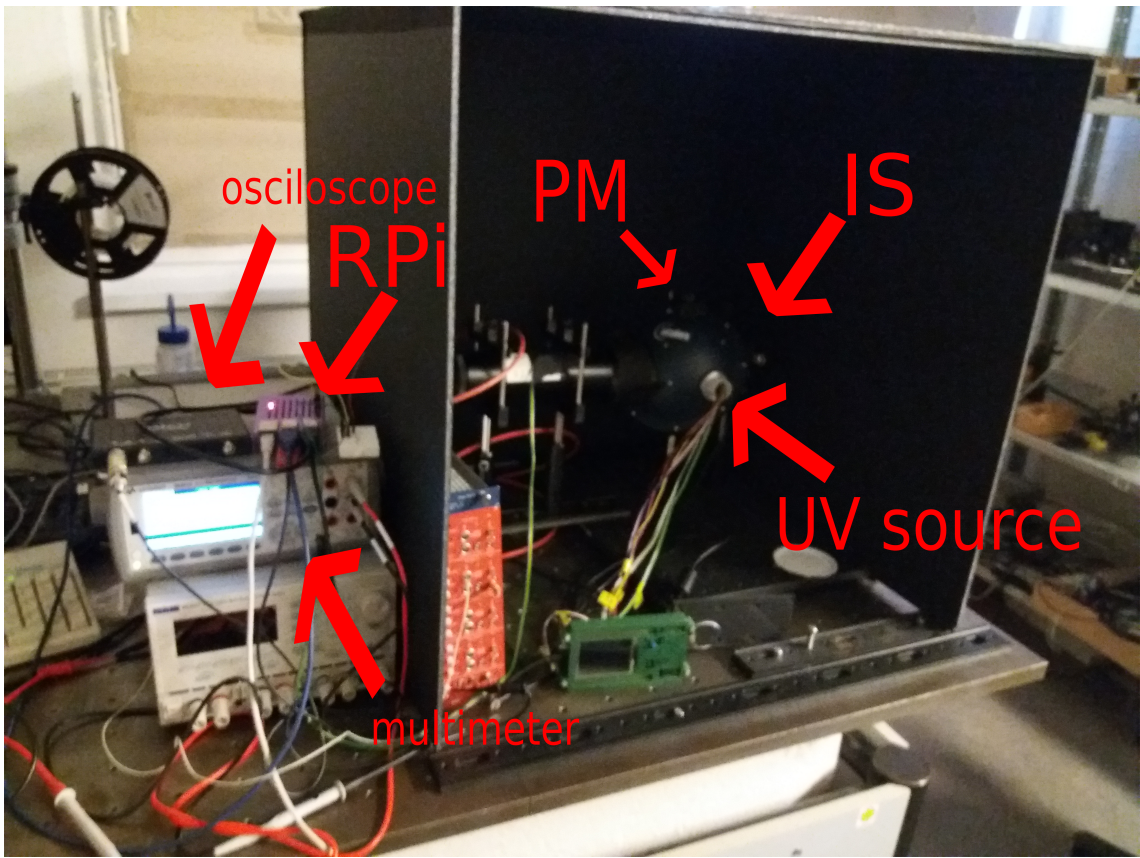


Figure 5.3: Measuring apparatus.

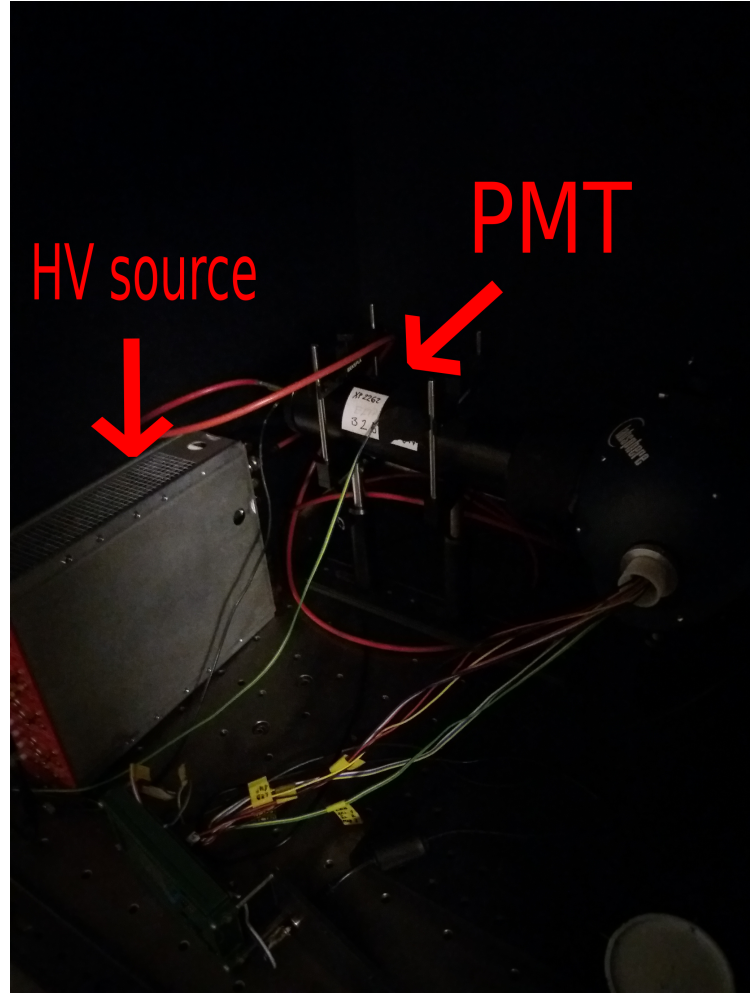


Figure 5.4: PMT mounting and HV source.

5.2.2 Data acquisition and analysis

All the data are taken in specified interval (15 or 30 minutes). Two files are produced - oscilloscope waveform file and a file with 30 samples of power meter, multimeter and a thermometer readings. From these 30 samples we calculate average and error. Most of data analysis we perform is done by C/C++ Root framework.

The data from oscilloscope contains the square pulses with noise (fig. 5.5). From them we need to extract the information of pulses height, slope and time of the rising edge.

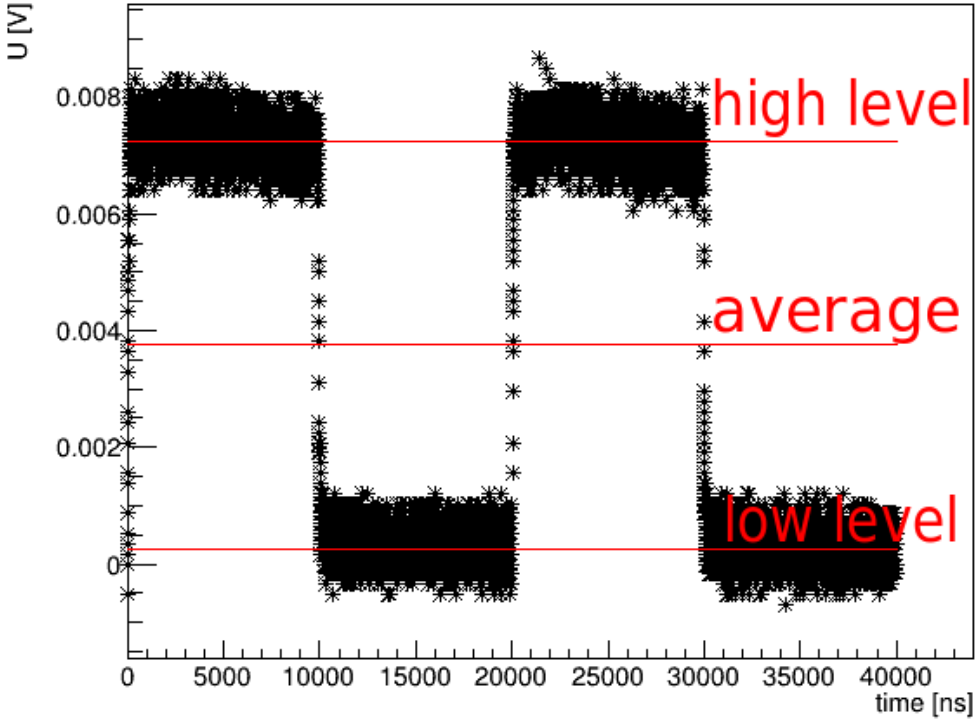


Figure 5.5: Determining the basic pulse properties - average, low and high levels of signal.

To determine the pulse height, we need to calculate the average value from all the samples at first. Then, we split the samples into two subgroups according to fact, whether they are higher or lower than the average. These subgroups are converted to histograms with fixed binning (around 5000 bins). These histograms are then fitted by gaussian. The means of these two fits determine two levels of the pulse - high (U_h) and low (U_l). The fig. 5.5 shows the real pulse with levels determined by this method. The height of pulse is then simply calculated by subtracting two levels: $U_H = U_h - U_l$.

The properties of the rising edge can be specified by two parameters, which we are able to extract from our data - time and the slope of the rising edge. We are able to calculate both of them if we identify the samples of the rising edge. These samples' values should be between 20 % and 80 % of the U_H . First, we need to detect the rising edge in waveform data sequence. However, the signal is very noisy and this can not be simply done by detecting the exceeding of the 10 % of the U_H . To achieve that, we cycle through the waveform until we meet two conditions - the value is higher than average (and lesser than 80%) and the derivative is positive. Due to the noise, the derivative could not be calculated from two or three points, thus we use Savitzky–Golay polynomial's derivative at chosen point: $y' = \frac{1}{12h}(y_{i-2} - 8y_{i-1} + 8y_{i+1} - y_{i+2})$. However we care only of positive/negative sign, so $\frac{1}{12h}$, where h is the small step, is no use for us. When these two conditions are met at some point, the program cycles back from the point through the waveform until reaches 20% level, and then beginning at the same point, which met the conditions, cycles up to reaching 80% level. All the samples traversed by this way are considered as samples of the rising edge. The rising time is

calculated simply by multiplying the number of these samples by the sample time (2 ns). The slope is calculated from linear fit of these samples (fig. 5.6).

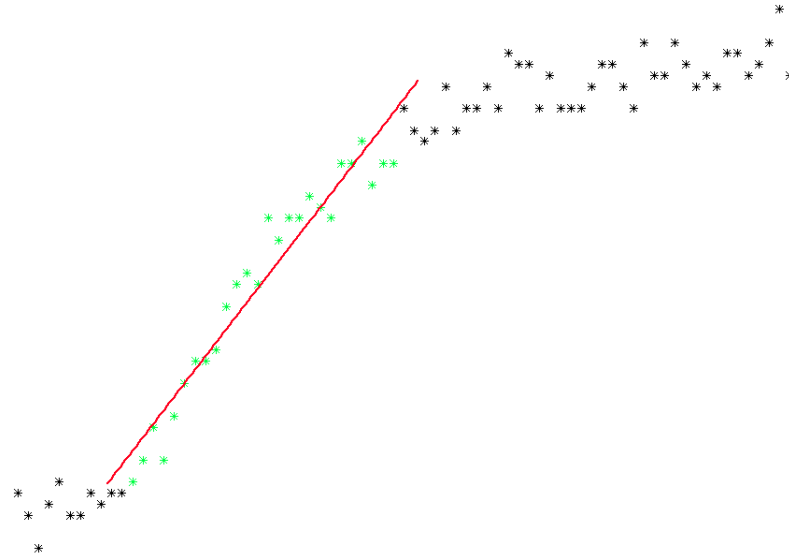


Figure 5.6: Linear fit of rising edge points (marked as green).

5.2.3 Results

First data taking sequence ran about two weeks. Taken data were analysed by methods described in previous chapter and results are presented in the following graphs. The first two graphs describe optical power with respect to time (first from PM and second is the PMT pulse height).

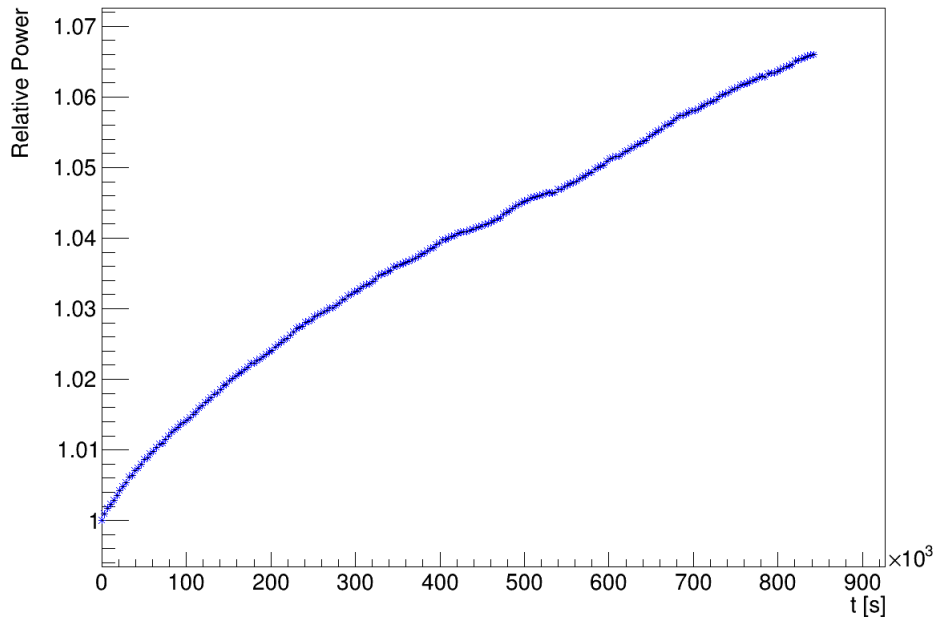


Figure 5.7: Time evolution of optical power.

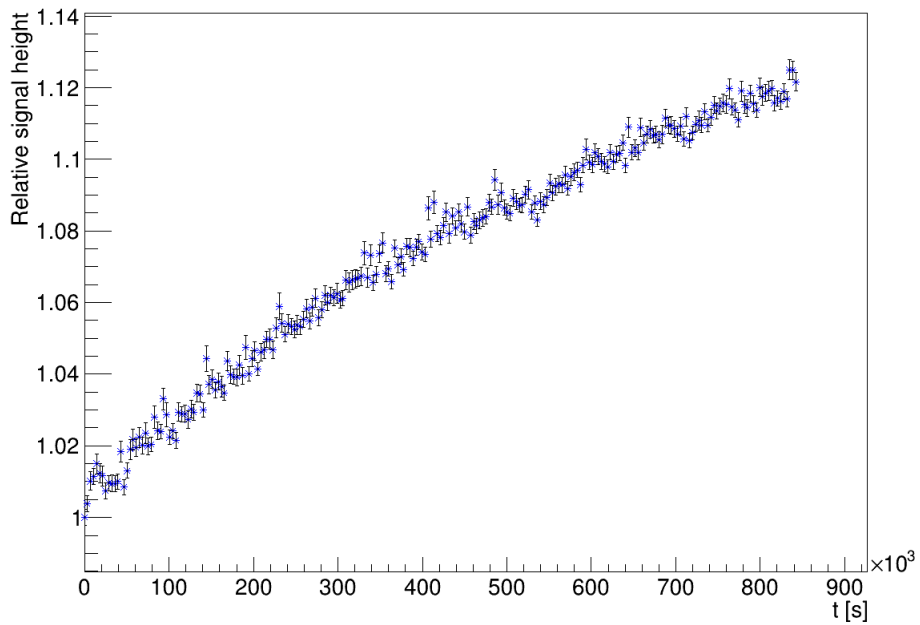


Figure 5.8: Time evolution of the pulse's height.

In the next two graphs we present calculated heights and slopes.

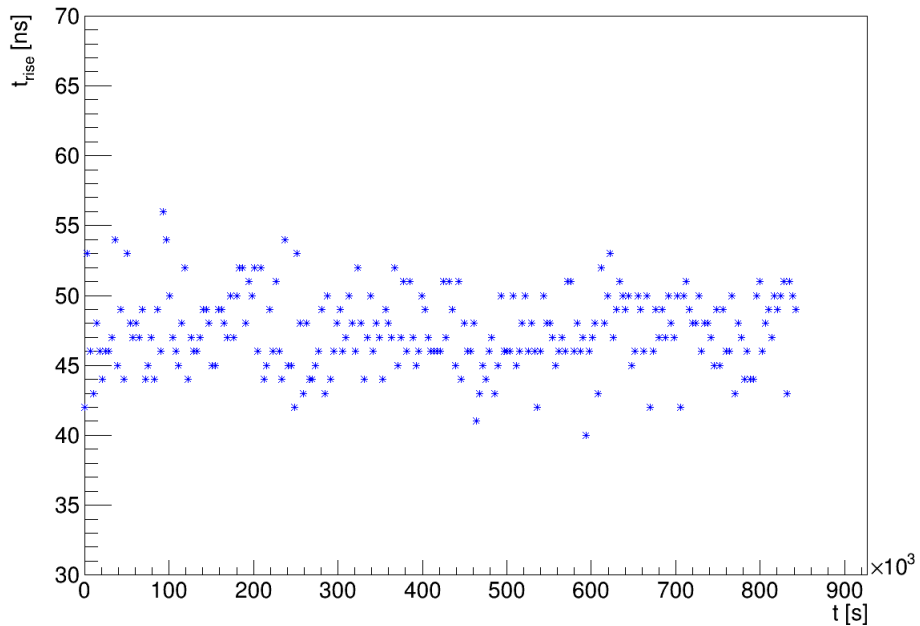


Figure 5.9: Time evolution of the pulse's edge rise time.

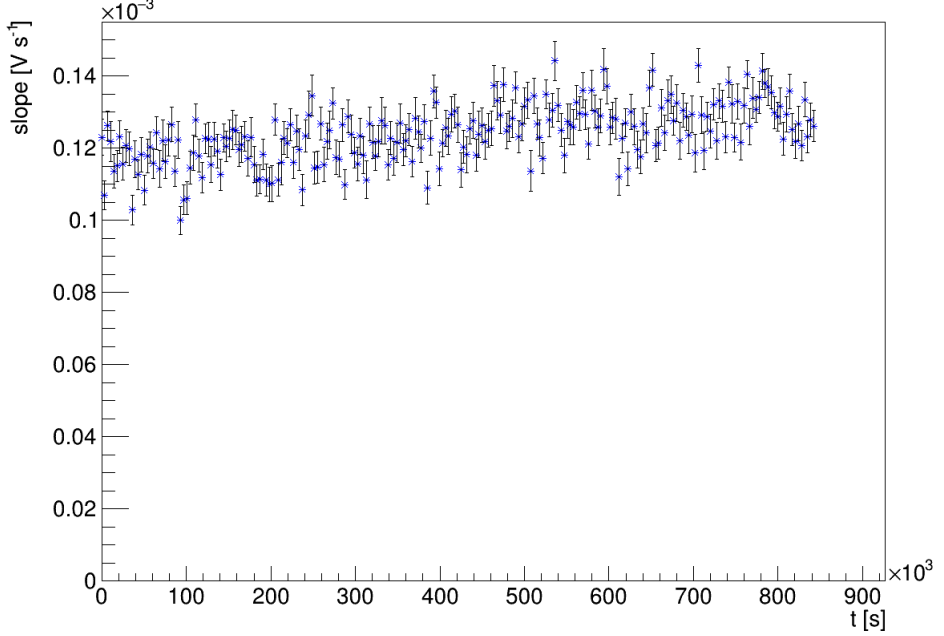


Figure 5.10: Time evolution of the pulse's edge slope.

We also measured PMT's temperature for potential gain changes.

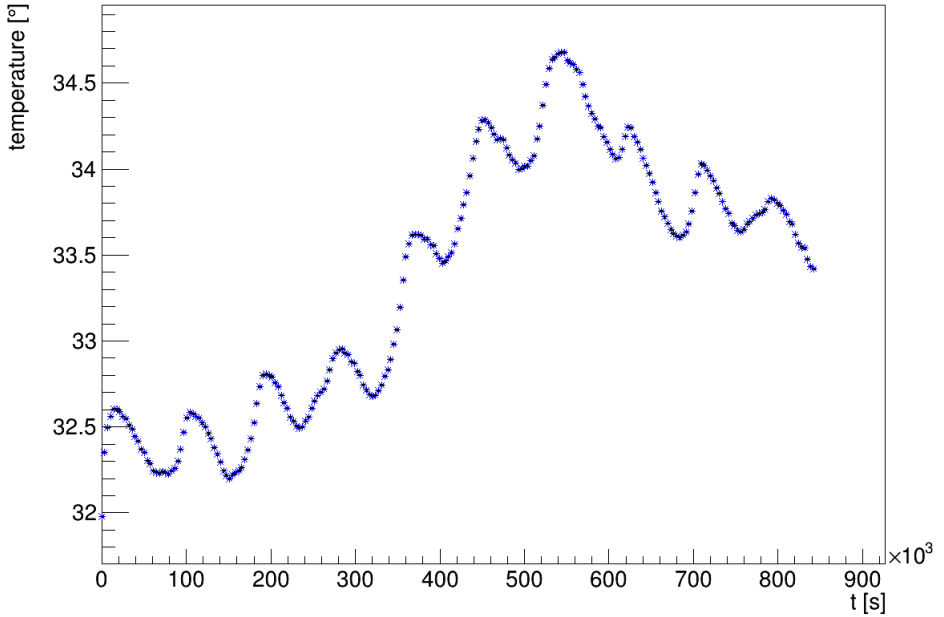


Figure 5.11: Time evolution of the PMT's temperature.

From analysed data we may observe that the power is rising over time. This fact is confirmed by two sensors - both PM and PMT. In case of PMT there may be the drift in gain over time. Gain drift may be caused by changes in voltage (equation 4.2) or in temperature. In case of temperature, the trend is not only rising as U_H 's trend does, so the 2° change in temperature may play little role in U_H increase, but it is not

probably the main cause of this effect. The graphs 5.9 and 5.10 shows that pulse is not deforming over time.

The optical power instability may be caused by failures in LED driving circuit (changes in current flowing by diode) or by ageing processes in the UV diodes. The PM shows that the power increase is around 7% in 10 days, which is unacceptable for any calibration source.

To confirm this measured fact and check for possible causes of the optical power instability we repeated this measurement by few times with similar results. But during these measurements we used multimeter to monitor PMT's voltage. For measuring the current flowing by the diode in the internal current source circuit, we used the second channel of the oscilloscope.

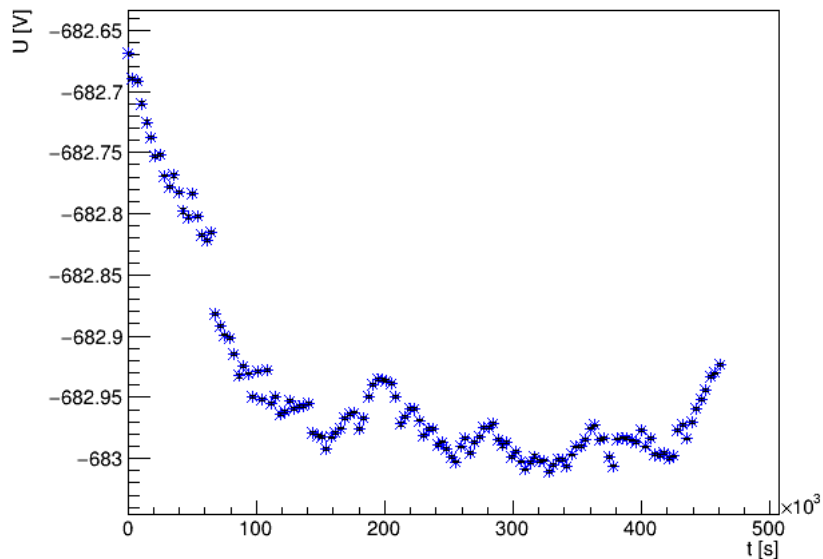


Figure 5.12: Time evolution of the PMT's voltage.

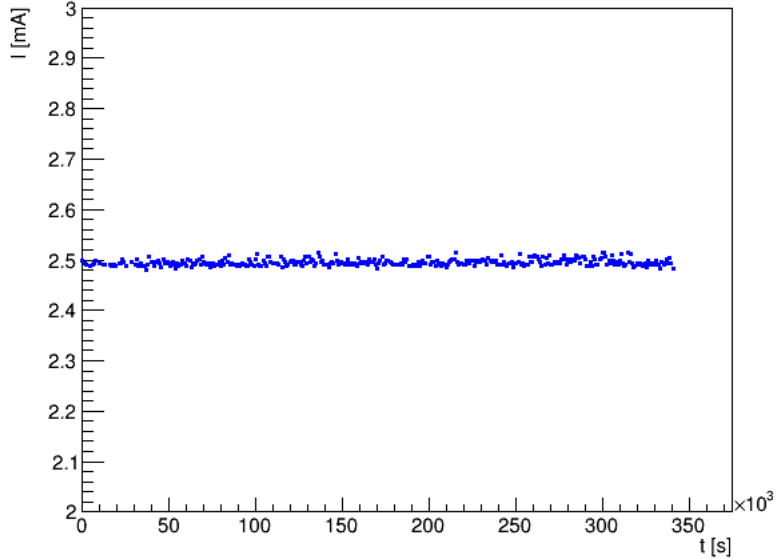


Figure 5.13: Time evolution of the UV LED's current.

Other measurements of optical power have ended in similar way. But by using the multimeter we can see that PMT's voltage is stable (fig. 5.12). It is varying only about 0.4 V at the beginning.

The measurement of current by oscilloscope was done and analysed in similar way as was done for the PMT's pulses. Both of them are PWM square pulses by shape. The oscilloscope's probe was connected to the 100Ω resistor, which is in serial to the LED and the current source and acted as a simple U/I converter. As we can see in fig. 5.13, the current varies only a little over the value which was set ($I_d = 2.5$ mA), and thus the rising trend of optical power is definitely not caused by the current variations.

5.3 UV LED diode ageing

As was seen in results of previous measurements, the diode ageing process is the most probable cause of the changes in optical power. We tried to confirm this fact by ageing the similar UV LED (type MT3650W3-UV).

The single UV LED powered by the current source lm334 on $I_d = 7.1$ mA was mounted onto IS's port and the optical power in continual mode was measured by the PM16. For the additional correction - the I_d was also measured by keysight multimeter.

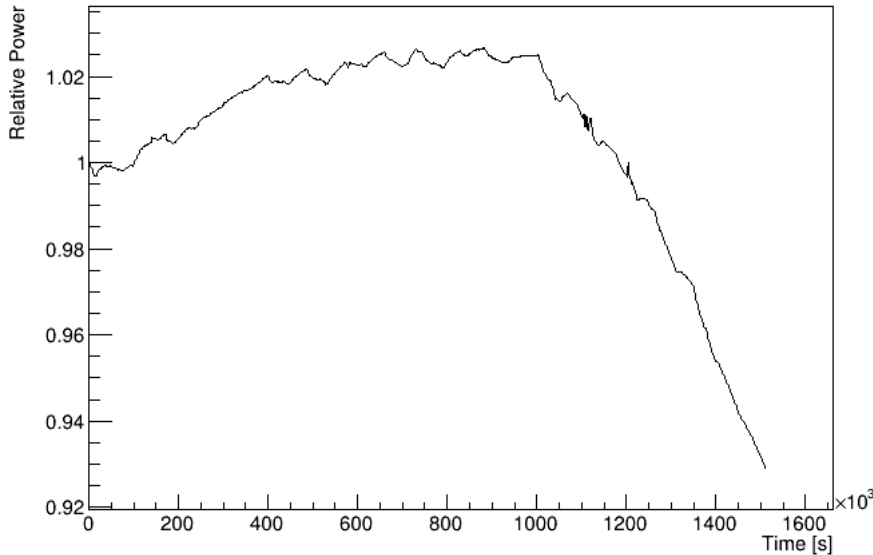


Figure 5.14: Time evolution of the optical power of single UV LED.

On the fig. 5.14 we can see that the optical power of single LED increased about 2% after one week. Then followed a stable interval which lasted about a week, but after that period the LED started "dying" and the power started to decrease.

There are 2 major possibilities to fix the LED power variation problem. The first possibility is to monitor the time usage of the UV source and according to that recalibrate the source, but the behaviour may vary diode from diode and thus it has many disadvantages. The second and more accurate approach is to regulate the power by an optical feedback.

5.4 Optical feedback - potential fix

One way to handle the ageing process of UV LED diodes is to monitor the power and according to the changes set the diode current I_d . To achieve that, we tried to develop a prototype of optical feedback concept, which is based on detection UV photodiode.

The part of optical power is reflected from LED to photodiode. Photocurrent induced this way is converted to voltage which is read by ADC (analog-digital converter). This information is then used by the STM32 board to adjust the current level by DAC. One problem is that the optical power is delivered in pulses, and thus it is necessary to sample these pulses and determine the height.

5.4.1 Detection photodiode

As detection photodiode which we chose is GUVV-T10GD. It is guaranteed to be UV-A sensor with wavelength responsivity from 230 to 395 nm. However, it is necessary to test more of its properties, because some of the properties, which are essential for our application, are not shown in datasheets and probably haven't been yet measured - temperature dependency of the dark current, responsivity to 10 μ s square signals and ageing processes. The reverse voltage of photodiode U_r could go up to 2 V. With higher the U_r is, the lower is the diode's capacity.

Dark current

Information of dark current is very important. We need to know if the signal levels are much greater than dark current. We measured dark current with 7 set temperatures. Current was measured by Keithley 2470 picoammeter. Temperature was set by autoregulated transistor heating plate. The transistor plate is driven by STM32 nucleo's DAC. The nucleo is controlled by the RPi. The RPi also communicates with picoammeter and controls the entire data acquisition. We measured two series - one with reverse voltage $U_r = 0.1$ V and second with reverse voltage $U_r = 1$ V. The picoammeter is also capable of adjusting voltage, so it was used as a source of reverse voltage.

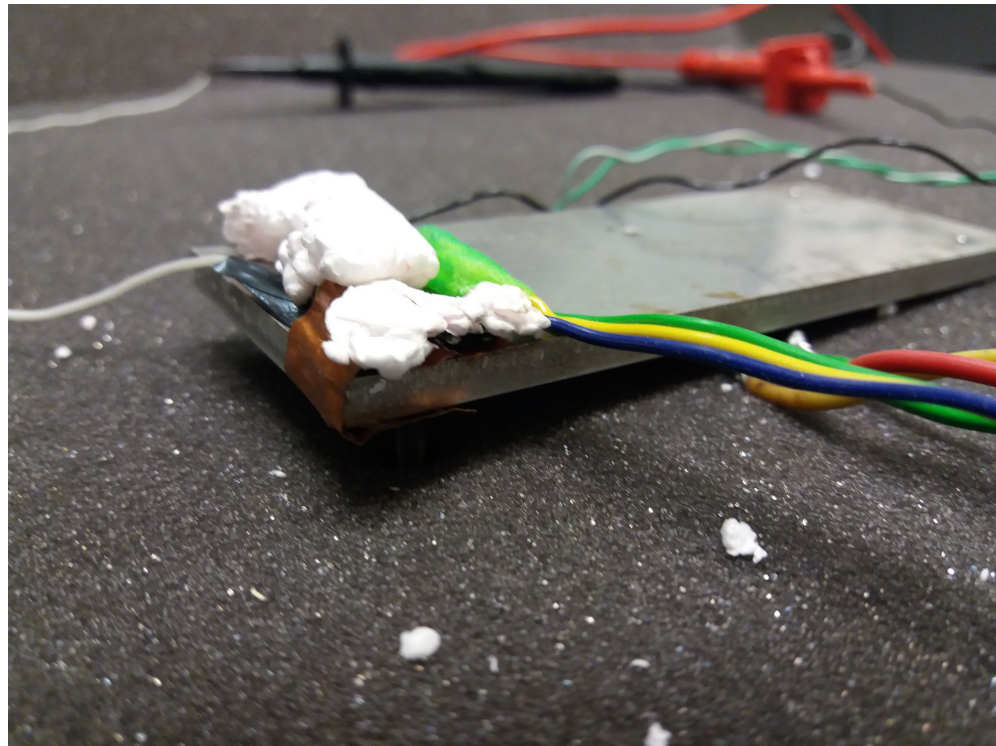


Figure 5.15: UV detection diode mounted on heating plate, covered by insulating material. The thermometer is mounted next to it.

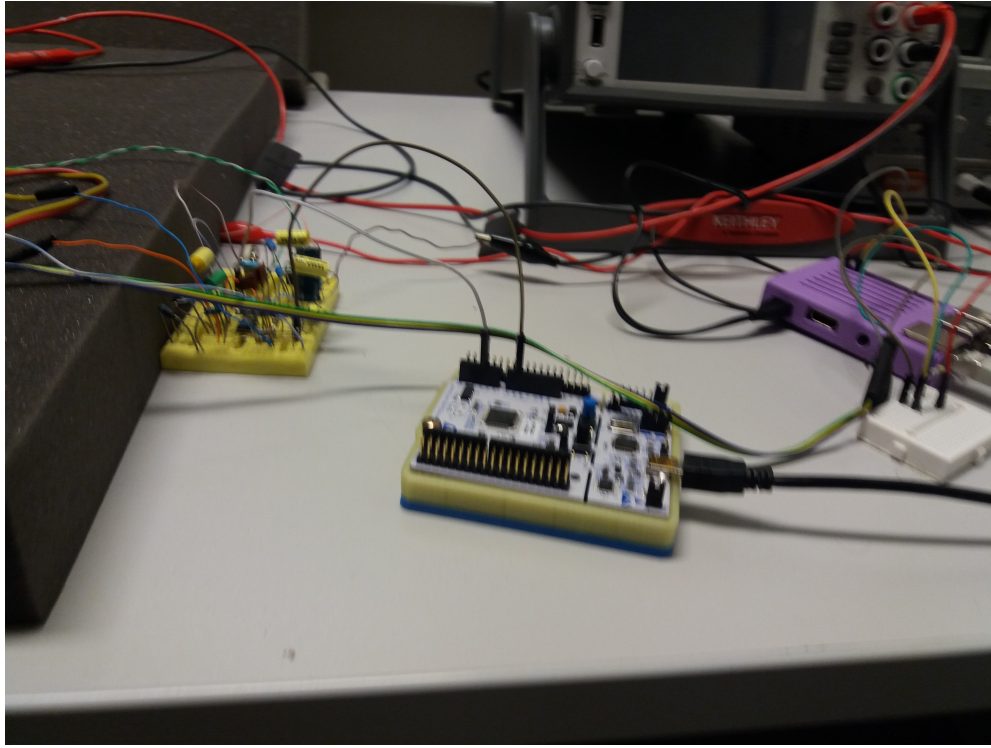


Figure 5.16: Heating control and measurement control. From the left - heating circuit, STM32 nucleo, RPi

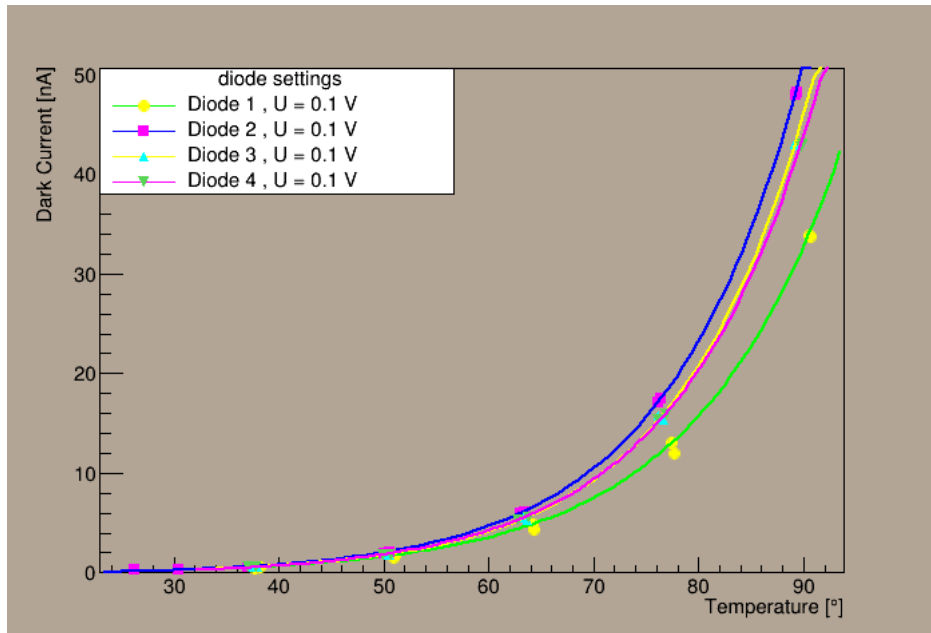


Figure 5.17: Dark currents with the reverse voltage $U_r = 0.1$ V.

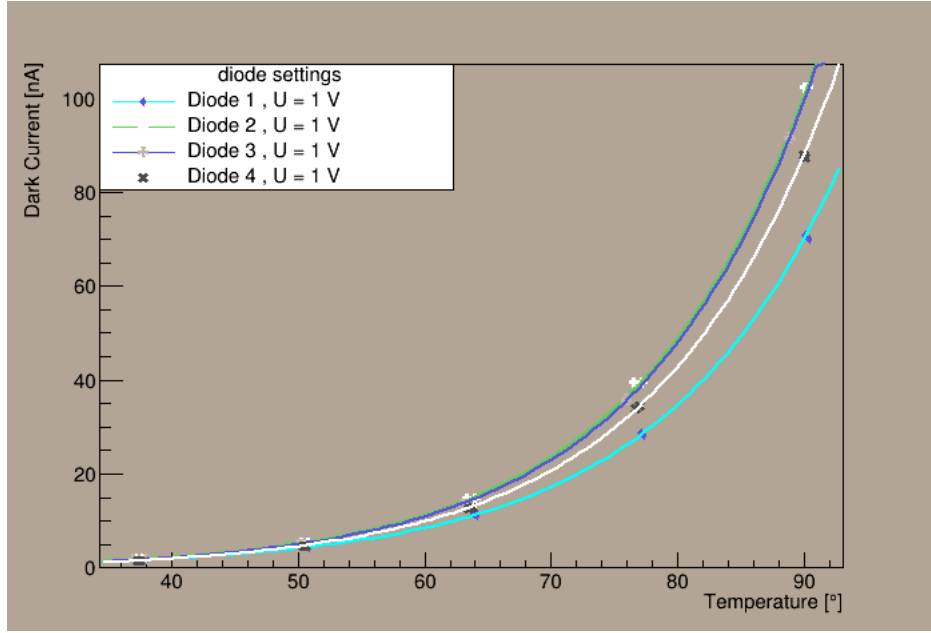


Figure 5.18: Dark currents with the reverse voltage $U_r = 1$ V.

We measured 5 diodes. However, the dark currents of one diode were on abnormal level, and that's why its characteristics are not plot in graphs with others. This diode was not suitable for our application.

From the measured data we can see, that for the expected operating temperatures ($t < 50^\circ C$), the dark current is $I_{dark} < 10$ nA.

Signal responsivity

By direct illumination of the photodiode by the UV LED ($I_d = 7.5$ mA) we are able to induce photocurrent about $I_p = 5 \mu A$, which is of the higher order than the measured dark current.

To test responsibility of the square pulses, we integrated the photodiode into the I/U trans-impedance amplifier with the op-amp ADA4805 with feedback parameters $R_F = 100$ k Ω and $C = 9$ pF. We illuminated the photodiode by the UV LED connected to the square pulse generator. The response could be seen on fig. 5.19.

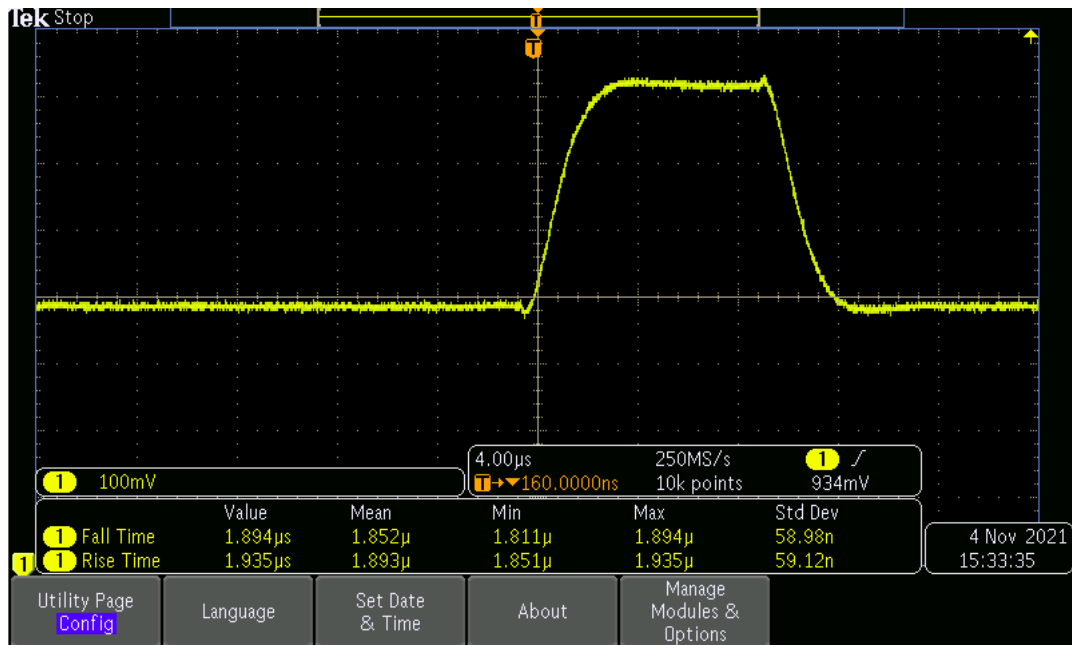


Figure 5.19: Photodiode's response on 10 μ s square pulse.

This way we are able to see the pulsing UV LED light. However, the rising edge of feedback pulse is deformed.

Artificial ageing

For the feedback photodiode, the time stability is very important. It has to last much more than the LED. To test the long-time stability, we tried to artificially age the feedback photodiode. It is well-known fact from the molecular physics, that the diffusion coefficients of most materials depends on temperature and they grow with increasing temperature. So we tried to speed up the ageing by holding the photodiode under the maximum of operating temperature (on 80°C) for one week. During that period, the photodiode was illuminated by UV LED and the photocurrent was measured (fig. 5.21).

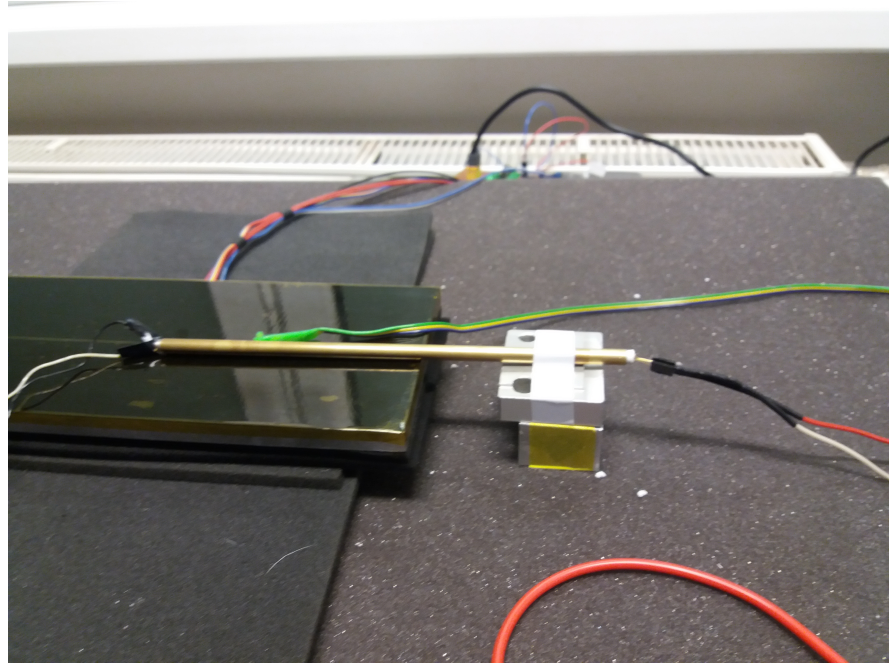


Figure 5.20: Photodiode mounted on bigger transistor heating and illuminated by LED through pipe.

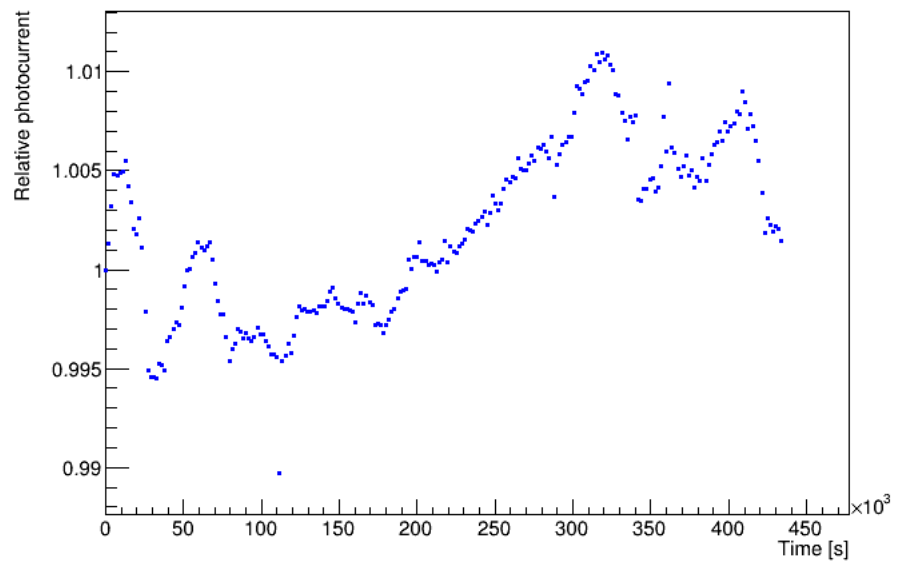


Figure 5.21: Time evolution of the photodiode's photocurrent.

The time evolution shows that the photodiode's photocurrent increased around 1 % over one week. However, this small variation is probably caused by the LED ageing, as was shown before.

Due to the fact, that any bigger drift in sensitivity was not observed under the bad conditions, we come to a conclusion that the feedback photodiode is much more stable than the LED.

5.5 Modified UV source for drone mounting

Chapter 6

Monitoring system

As was mentioned before, the quality of the fluorescence detection depends on atmospheric conditions and a durability of detection parts is also dependent on exposure to these effects. Thus it is highly advised to monitor them and plan shifts according to these conditions. To capture atmospheric data, we constructed a monitoring system - a meteostation, which we describe in this chapter.

6.1 Monitoring of multiple FAST telescopes

The main goal was to develop a monitoring system for multiple FAST telescopes, which is capable of acquiring data of temperature, humidity, wind speed and direction, raining and light exposure. These data have to be easily accessible, so it is necessary to store them in some database, which could be accessed throughout the network.

One of the requirements was also the modularity. Additional sensors and boards has to be integrated into system without requiring the core rework the of reading scripts.

The data could be used by operator when controlling the telescope or later in a complex analysis of detection events and calibration measurements. For example, the operator must be sure that there is no light source outside before he executes command to open the shutter of the telescope's hut. To obtain this information, he checks for the measured value from an ambient light sensor, which is a part of monitoring system.

6.2 Control units and sensors

Central control unit is a RPi, which collects data from other STM32 nucleos. For every FAST telescope there is one STM32 nucleo equipped with sensors, which is connected to the RPi via CAN bus. The operation scheme could be seen on (fig. 6.2). The RPi itself takes care of ultrasonic wind sensor and a rain sensor, because both wind and rain are same for every telescope. The Nucleos have connected dallas DS18B20 thermometers (1-Wire), BME230 temperature, humidity and pressure sensor(I2C) and an ambient light sensor (OPT3001) through an optoclick module. Additional possibility is also to include induction sensor catch failures in shutter opening/closing.

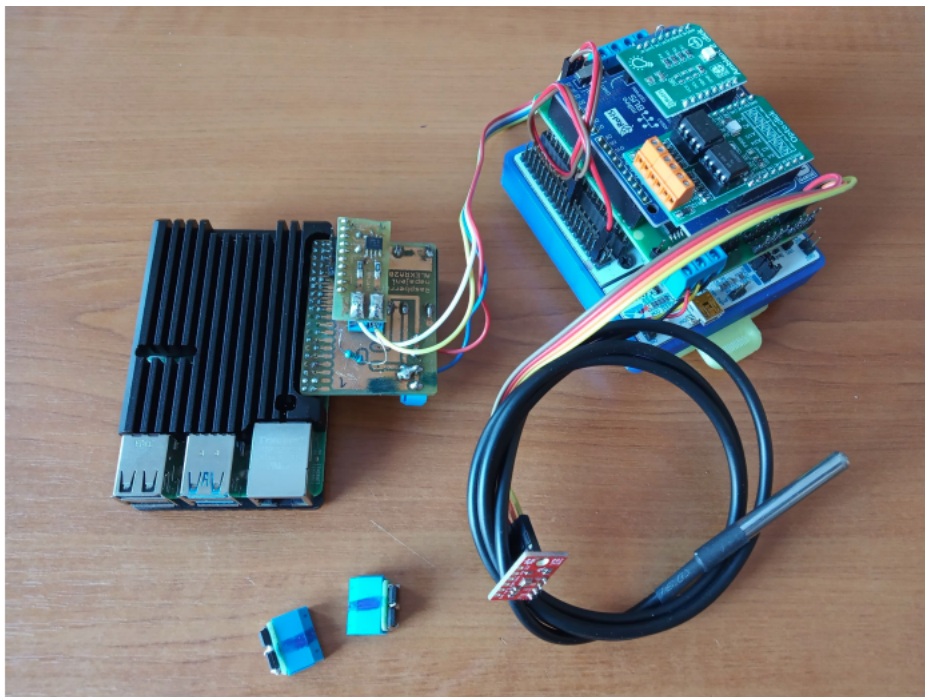


Figure 6.1: RPi and STM32 with sensors.

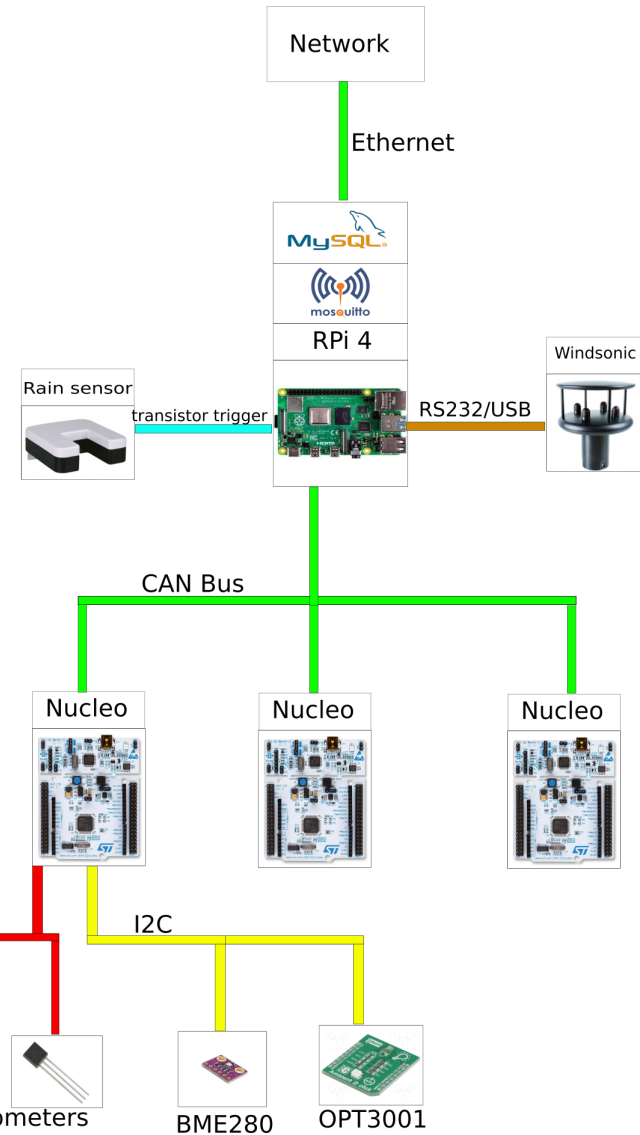


Figure 6.2: Operation scheme of the monitoring system.

6.3 Software system

For this application, where it is not essential to achieve fast sampling and do some fast responses, we decided to use python for RPi and micropython for STM32 nucleos. These languages offer us libraries and easy programming for some of our sensors, however in a cost of speed and memory (compared to C/C++ for example).

The data reading scripts are scheduled by classic linux's tool - crontab.

The main part of software communication between RPi (and RPi's internal processes) and STM32 nucleos is done through the MQTT Mosquitto server, which runs on RPi. Nowadays the MQTT is a useful service used in automatization processes, where the many messages from various devices are sent and received simultaneously. The processes could have three roles - publisher, subscriber and broker (in our case done by MQTT itself). The publisher process sends data packet with theme to broker. The broker calls all subscribers of this theme and passes them the data packet [13]. The processes must be programmed to communicate with MQTT service, which could be done by using various MQTT libraries. The MQTT scheme could be in our case

specified in following way: The running scripts (representing processes for MQTT) for data acquisition (Wind, rain, nucleo data transfer) are programmed as publishers and publish values of specified sensors with theme related to their names and types in specified intervals. The script, which handles the data transfer to a database is programmed as a subscriber.

The data are in specified intervals picked up from MQTT, and transferred into a MySQL database. The MySQL database is a part of RPi's MySQL server, and thus the data could be easily read by any other device in internal network. This database data could be also used for some web browser application to visualize the time development of local weather conditions.

The modularity is achieved by configurations files, which describe the scheme of the connected sensors and the data acquisition. In case of upgrade - adding of an additional sensor or an another nucleo board, it is not necessary to rewrite any of the reading scripts. The configurations files are the only part which has to be changed.

Usage of this scheme, where the processes are separated and executed in scheduled times by operating system makes the system tolerant for many faults (both sensors' and nucleos' HW and SW failures) and eases the potential future upgrades.

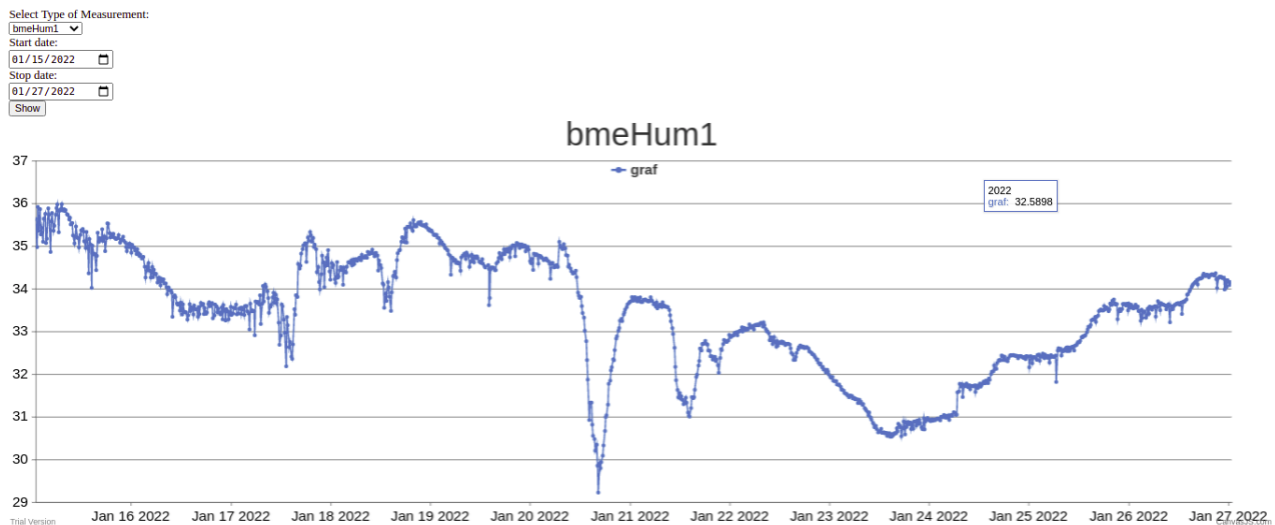


Figure 6.3: View of the web interface, which allows to access and visualise the measured data stored in databases, graph created by using javascript libraries [6].

Chapter 7

Calibration data analysis

In this section we present the analysis of calibration data, which we acquired by illuminating one FAST telescope (Argentina) by the older version of homogeneous UV LED source mounted into the IS. The older version of UV source was incapable of generating exact square pulse, and thus its output is deformed. However, the pulse's shape is stable and thus it was possible to use it for this experiment.

The main goal of this experiment is to obtain the relative responsivity ration constants for every of the four FASTs' PMTs (pixels) with respect to the pixel with greatest response for three positions of illumination - from left, right and bottom. Full specifications of the pixels numbering and positions could be seen on fig. 7.1.

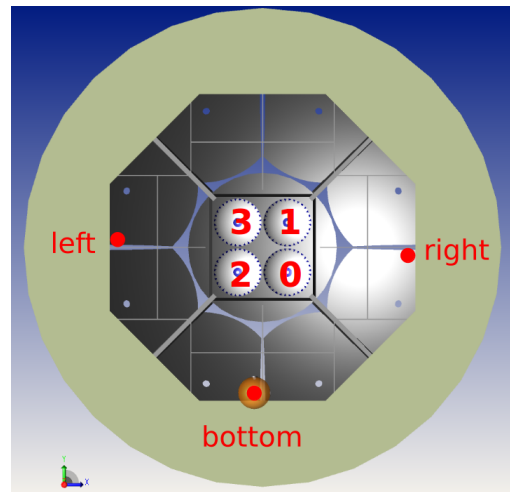


Figure 7.1: Orientation of FASTs' PMTs (pixels).



Figure 7.2: UV LED source mounted onto telescope.

7.1 Calibration process

The UV source was mounted onto three positions and used as EULS to generate 8 μs pulses. Two LED current levels were tested - $I_{d1} = 0.3 \text{ mA}$ and $I_{d2} = 0.8 \text{ mA}$. These pulses trigger an event for the telescope - it acquires waveform data from every of the four PMTs. The PMTs' signal is converted into the number of photoelectrons registered in 20 ns. The example of detected 0.3 mA pulse from bottom position can be seen on fig (7.3). The 0.8 mA pulse is on fig. (7.4).

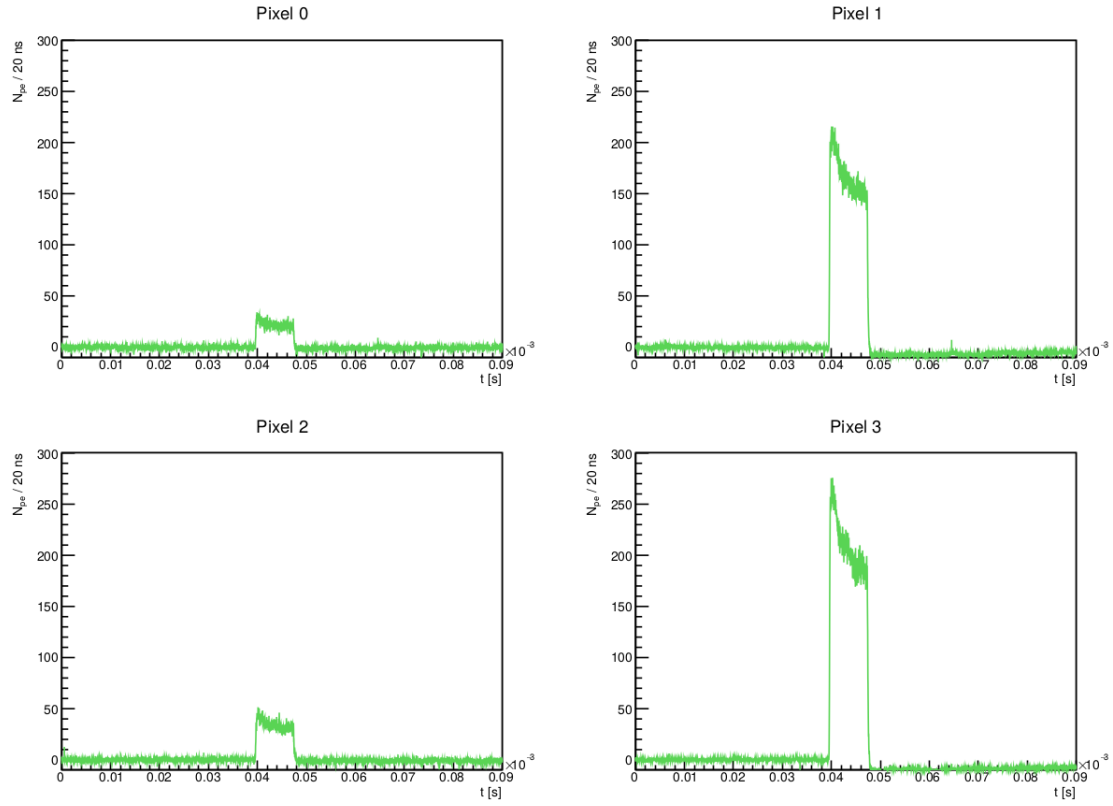


Figure 7.3: 0.3 mA pulse registered by all pixels.

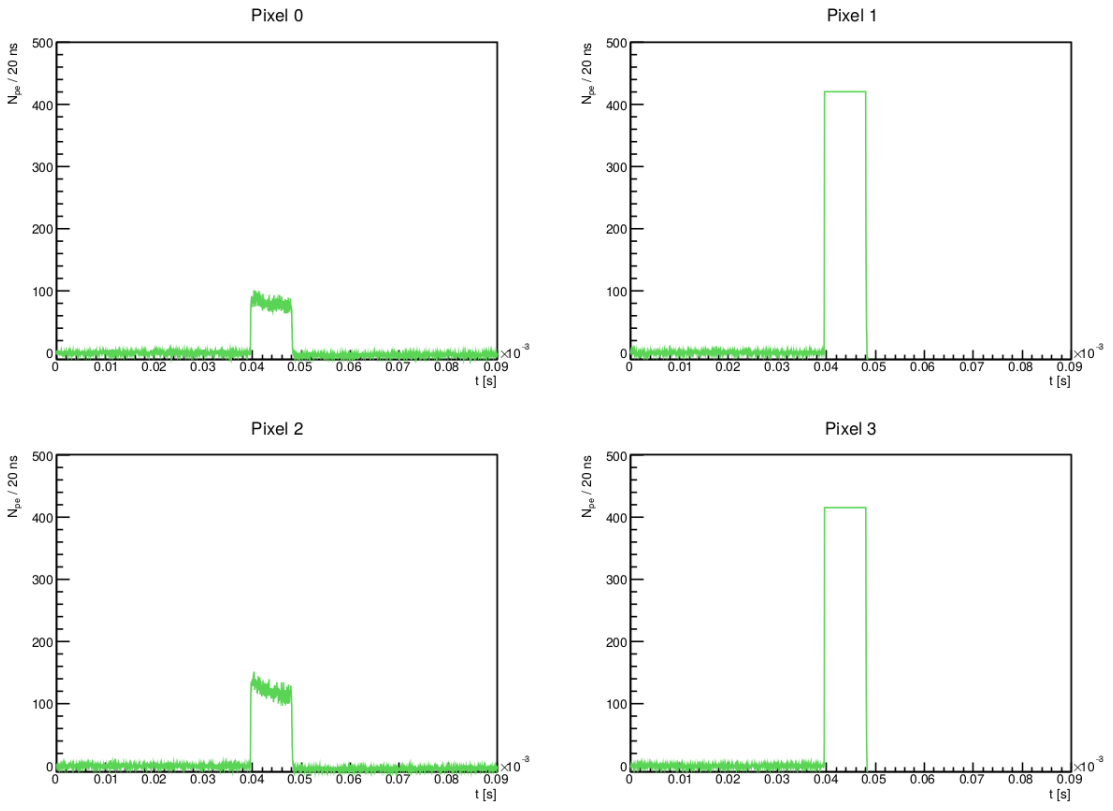


Figure 7.4: 0.8 mA pulse saturated two pixels.

The fig. 7.4 shows that the 0.8 mA pulse saturated the pixel 1 and 3 and thus it is not possible to use them in analysis.

The 0.3 mA pulses are suitable for our analysis. However, due to their deformation we are not able to use analogous analysis scheme as we did for calibration source testing. The best parameter describing the collection efficiency of the PMT is the pulse's integral.

7.2 Analysis and results

The data includes 4 waveforms for every detected pulse event and consists around 800 pulse events (for every position). From these signal waveforms we calculate the pulse's integral and then use these signal integrals to construct histograms. These histograms are fitted by gaussian. This process is repeated for all the three positions.

The fitted histograms can be seen on fig. 7.5 (left), 7.6 (right) and 7.7 (bottom).

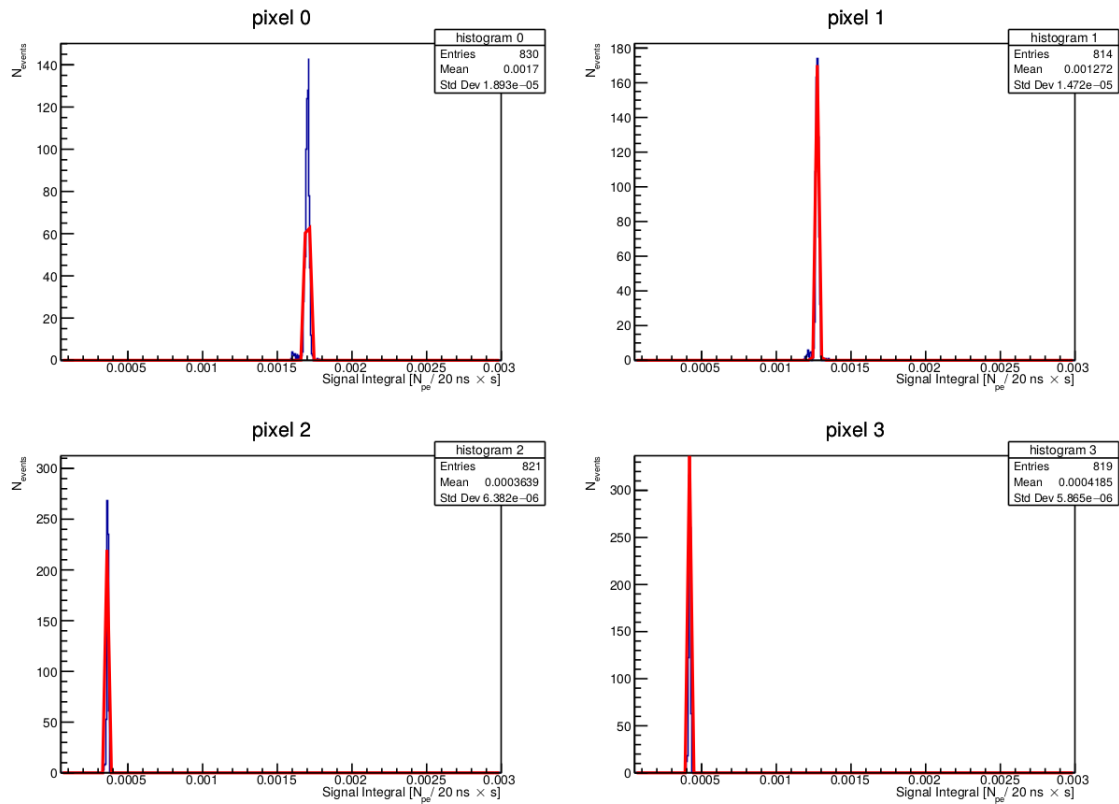


Figure 7.5: Signal integral histograms with gaussian fits for left position.

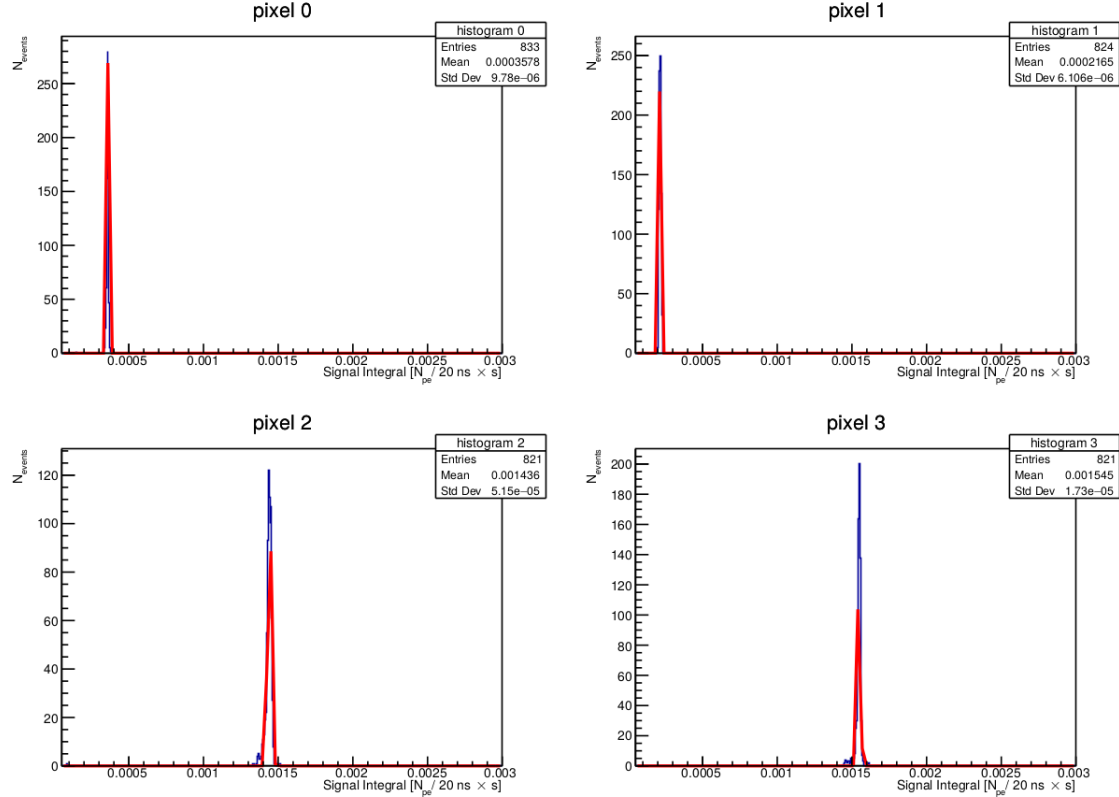


Figure 7.6: Signal integral histograms with gaussian fits for right position.

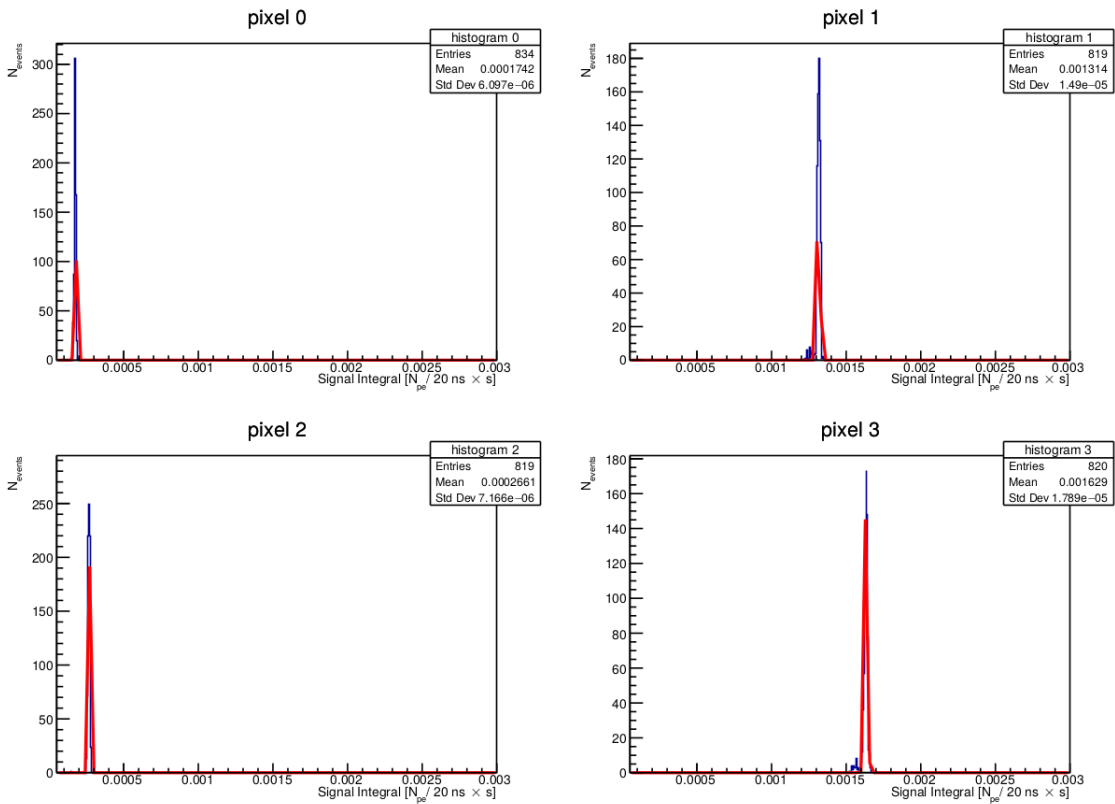


Figure 7.7: Signal integral histograms with gaussian fits for bottom position.

The main parameter for determining responsivity ration constants is the mean value of the signal integrals, which is extracted from the gaussian. The relative calibration constants are calculated as follows:

$$c_i = \frac{m_i}{m_{\text{ref}}}. \quad (7.1)$$

Where c_i is a relative responsivity ration constants for i-th pixel, m_i - associated mean value and m_{ref} - mean value of the reference pixel. As the reference pixel is chosen the one with the greatest responsivity.

The associated error is:

$$\mu(c_i) = c_i \sqrt{\left(\frac{\mu(m_i)}{m_i}\right)^2 + \left(\frac{\mu(m_{\text{ref}})}{m_{\text{ref}}}\right)^2}. \quad (7.2)$$

As the basic errors $\mu(m_{\text{ref}})$ and $\mu(m_i)$ are taken only the errors from the gaussian fits. Other systematic uncertainties were not yet determined and are not considered in this thesis.

The results calculated by these equations for every position can be seen in the following table.

	right	left	bottom
c_0	0.2314 ± 0.0002	1	0.1070 ± 0.0002
c_1	0.1397 ± 0.0002	0.7485 ± 0.0003	0.8061 ± 0.0003
c_2	0.9304 ± 0.0004	0.2138 ± 0.0002	0.1631 ± 0.0002
c_3	1	0.2462 ± 0.0002	1

Table 7.1: Table of calculated relative responsivity ration constants.

7.3 Simulation compartment and discussion

To discuss the relevancy of measured and calculated values, we compare them to their counterparts from optical simulations, which were designed by Mgr. Martin Vacula from SLO. These simulations consists of theoretical models of FAST's mirrors and pixels illuminated by EULS in same three positions as was defined before. These models includes inhomogeneity correction matrixes for every pixel.

	right	left	bottom
c_0	0.48	0.95	0.44
c_1	0.41	1	0.98
c_2	1	0.41	0.46
c_3	0.95	0.46	1

Table 7.2: Table of simulated relative responsivity ration constants by Mgr. Martin Vacula.

The compartment between the two tables (theoretical simulation - 7.2 and the real measurement - 7.1) shows that the two pixels, which are lesser illuminated at the specified position have lesser responsivity than they should have according to the simulations.

These differences may be caused by uncertainties in the EULS positioning, its partial space inhomogeneity, mirror inhomogeneity, or some yet undiscovered phenomena.

Conclusion

We are completely f***d.

Bibliography

- ¹L. Tománková, “Optical properties and calibration of the pierre auger fluorescence detector”, PhD thesis (Karlsruher Institut für Technologie (KIT), 2016), 208 pp.
- ²D. Mandat, M. Palatka, M. Pech, P. Schovanek, P. Travnicek, L. Nozka, M. Hrabovsky, P. Horvath, T. Fujii, P. Privitera, M. Malacari, J. Farmer, A. Galimova, A. Matalon, M. Merolle, X. Ni, J. Bellido, J. Matthews, and S. Thomas, “The prototype opto-mechanical system for the fluorescence detector array of single-pixel telescopes”, Journal of Instrumentation **12**, T07001–T07001 (2017).
- ³A. Haungs, D. Kang, S. Schoo, D. Wochele, J. Wochele, W. Apel, J. Arteaga-Velázquez, K. Bekk, M. Bertaina, J. Blümer, H. Bozdog, I. Brancus, E. C. Cantoni, A. Chiavassa, F. Cossavella, K. Daumiller, V. Souza, F. Di Pierro, P. Doll, and J. Zabierowski, “The kascade cosmic-ray data centre kcde: granting open access to astroparticle physics research data”, (2018).
- ⁴M. Malacari, J. Farmer, T. Fujii, J. Albury, J. Bellido, L. Chytka, P. Hamal, P. Horvath, M. Hrabovský, D. Mandat, J. Matthews, L. Nozka, M. Palatka, M. Pech, P. Privitera, P. Schovánek, R. Šmída, S. Thomas, and P. Travnicek, “The first full-scale prototypes of the fluorescence detector array of single-pixel telescopes”, Astroparticle Physics **119**, 102430 (2020).
- ⁵M. Vacula, P. Horvath, L. Chytka, K. Daumiller, R. Engel, M. Hrabovsky, D. Mandat, H.-J. Mathes, S. Michal, M. Palatka, M. Pech, C. M. Schäfer, and P. Schovanek, “Use of a general purpose integrating sphere as a low intensity near-uv extended uniform light source”, Optik **242**, 167169 (2021).
- ⁶canvasJS, *Canvasjs*, <https://canvasjs.com/>.
- ⁷F. collaboration, *Fast project*, <https://www.fast-project.org>.
- ⁸Hamamatsu: photomultiplier tubes basics and applications, https://www.hamamatsu.com/resources/pdf/etd/PMT_handbook_v3aE.pdf.
- ⁹S. Kliewer, *The compact cosmic ray telescope aboard the kuiper airborne observatory*, <https://cosmic.lbl.gov/SKliewer/Index.htm>.
- ¹⁰Photonis: photomultiplier tube basics, https://psec.uchicago.edu/library/photomultipliers/Photonis_PMT_basics.pdf.
- ¹¹T. A. project, *Telescope array project*, <https://www.telescopearray.org>.
- ¹²C. RNDr. Pavel Kolář, *Z velmi vzdálených galaxií*, Czech, <https://www.fzu.cz/aktuality/z-velmi-vzdalenych-galaxii>.
- ¹³R. Santos, *What is mqtt and how it works*, <https://randomnerdtutorials.com/what-is-mqtt-and-how-it-works/>.
- ¹⁴B. Skuse, *The riddle of ultrahigh-energy cosmic rays*, <https://physicsworld.com/a/the-riddle-of-ultrahigh-energy-cosmic-rays/>.

¹⁵P. Technology, *Picoscope ® 2000 series (a api) pc oscilloscopes and msos programmer's guide*, <https://www.picotech.com/download/manuals/picoscope-2000-series-a-api-programmers-guide.pdf>.